

NEW EQUATIONS OF STATE IN SIMULATIONS OF CORE-COLLAPSE SUPERNOVAE

M. HEMPEL¹, T. FISCHER^{2,3}, J. SCHAFFNER-BIELICH⁴ AND M. LIEBENDÖRFER¹

¹Departement Physik, Universität Basel, Klingelbergstr. 82, 4056 Basel, Switzerland

²GSI, Helmholtzzentrum für Schwerionenforschung GmbH, Planckstr. 1, 64291 Darmstadt, Germany

³Institut für Kernphysik, Technische Universität Darmstadt, Schlossgartenstr. 9, 64289 Darmstadt, Germany

⁴Institut für Theoretische Physik, Ruprecht-Karls-Universität, Philosophenweg 16, 69120 Heidelberg, Germany

Draft version October 22, 2018

ABSTRACT

We discuss three new equations of state (EOS) in core-collapse supernova simulations. The new EOS are based on the nuclear statistical equilibrium model of Hempel and Schaffner-Bielich (HS), which includes excluded volume effects and relativistic mean-field (RMF) interactions. We consider the RMF parameterizations TM1, TMA, and FSUGold. These EOS are implemented into our spherically symmetric core-collapse supernova model, which is based on general relativistic radiation hydrodynamics and three-flavor Boltzmann neutrino transport. The results obtained for the new EOS are compared with the widely used EOS of H. Shen et al. and Lattimer & Swesty. The systematic comparison shows that the model description of inhomogeneous nuclear matter is as important as the parameterization of the nuclear interactions for the supernova dynamics and the neutrino signal. Furthermore, several new aspects of nuclear physics are investigated: the HS EOS contains distributions of nuclei, including nuclear shell effects. The appearance of light nuclei, e.g., deuterium and tritium is also explored, which can become as abundant as alphas and free protons. In addition, we investigate the black hole formation in failed core-collapse supernovae, which is mainly determined by the high-density EOS. We find that temperature effects lead to a systematically faster collapse for the non-relativistic LS EOS in comparison to the RMF EOS. We deduce a new correlation for the time until black hole formation, which allows to determine the maximum mass of proto-neutron stars, if the neutrino signal from such a failed supernova would be measured in the future. This would give a constraint for the nuclear EOS at finite entropy, complementary to observations of cold neutron stars.

1. INTRODUCTION

Supernova explosions of stars more massive than $8 M_{\odot}$ are an active subject of research in astrophysics. The core-collapse supernova problem is related to the revival of the stalled bounce shock. It forms when the collapsing stellar core bounces back above normal nuclear matter density. Explosions in spherical symmetry have been obtained only for the low mass $8.8 M_{\odot}$ O–Ne–Mg core from Nomoto (1983, 1984, 1987) by Kitaura et al. (2006) and Fischer et al. (2010). More massive progenitor stars have extended high-density Si-layers surrounding the central iron core. The post-bounce evolution leads to a mass accretion period that lasts for several hundred milliseconds. For such iron-core progenitor stars explosions do not occur in spherically symmetric simulations. The bounce shock continuously loses energy by dissociation of heavy nuclei and neutrino heating is not sufficient enough to revive the standing bounce shock.

In addition to the standard scenario of neutrino-driven explosions (see Bethe & Wilson (1985)), several alternative explosion mechanisms have been proposed. These are the magneto-rotational mechanism by LeBlanc and Wilson (1970) and the acoustic mechanism by Burrows et al. (2006). All of which are working in multiple spatial dimensions. Multi-dimensional core-collapse supernova models, based on sophisticated neutrino transport approximations and general relativity, have become available only recently. These models have shown to increase the neutrino heating efficiency (see, e.g., Miller et al. (1993), Herant et al. (1994), Janka & Mueller (1996), Burrows et al. (2007)) and help

to aid the understanding of aspherical explosions (see, for example, Bruenn et al. (2006); Marek & Janka (2009); and Müller et al. (2010)).

Apart from the dimensionality, the simulations are also affected by uncertainties in the nuclear physics involved, which can be divided in weak processes and the equation of state (EOS). Changes in the nuclear physics input can have dramatic consequences and can even generate explosions in spherically symmetric models as was illustrated recently by Sagert et al. (2009) and Fischer et al. (2011). The authors explored the state of matter around and above nuclear matter density and investigated the possibility of the quark-hadron phase transition during the early post-bounce evolution of low and intermediate mass iron-core progenitor stars. It was found that the phase transition leads to the formation of a strong hydrodynamic shock wave which triggers the explosion. In the present article we study new aspects of the hadronic EOS and their consequences for the supernova dynamics.

Until today, there are only a few hadronic EOS available which cover a sufficiently large domain in density, temperature, and electron fraction so that they can be used in simulations of core-collapse supernovae. Usually, in such simulations the EOS is implemented in form of a table. The most prominent among them are the two “classic” EOS from Lattimer & Swesty (1991) (LS) and H. Shen et al. (1998a,b) (STOS) which are commonly used in computational astrophysics. The LS EOS is provided in form of programming routines for three different values of the nuclear incompressibility K of 180, 220, and 375 MeV. STOS is an EOS in tabu-

lar form which was calculated for the relativistic mean-field (RMF) model TM1 (Sugahara & Toki 1994). There has been a lot of progress for the supernova EOS in the last years. Recently, the new hadronic EOS tables of G. Shen et al. (2011b,a) became available, which are based on the virial expansion and two different RMF interactions in the Hartree approximation. In their first article they applied NL3 (G. Shen et al. (2011b)), followed by a table for FSUgold (G. Shen et al. (2011a)). Furthermore also an update of the original STOS EOS table appeared which has improved resolution, accuracy and grid-spacing (H. Shen et al. (2011)). In this article also another table was presented in which lambda hyperons are taken into account. Similarly, several other extensions of the STOS table are available, either with the formation of hyperons (Ishizuka et al. 2008) or the inclusion of the QCD phase transition (Nakazato et al. 2008; Sagert et al. 2009; Fischer et al. 2011). In the present investigation we apply the new EOS tables of Hempel & Schaffner-Bielich (2010).

An important aspect of the supernova EOS is the formation of light nuclei and their properties in the hot and dense medium. Note that the two classic supernova EOS include only alpha particles of all possible light nuclei, which are implemented with excluded volume effects. Typel et al. (2010) use a generalized RMF and a quantum statistical model (Röpke 2011) to study supernova matter taking into account the most important light nuclei with mass number $A \leq 4$. Significant differences in the composition were found compared to STOS, similar as in the recent studies of Horowitz & Schwenk (2006), O’Connor et al. (2007), Sumiyoshi & Röpke (2008), Heckel et al. (2009), and Hempel & Schaffner-Bielich (2010). Also thermodynamic variables, like ,e.g., the symmetry energy, are modified due to the appearance of light nuclei. A comparison between the excluded volume approach with all light nuclei, which is also used in the HS EOS, and the quantum many-body approaches of Röpke (2011) and Typel et al. (2010) is given by Hempel et al. (2011). It is found that the dissolution of light nuclei happens at similar densities and that the excluded volume approach gives an acceptable representation of the real microscopic medium effects, like, e.g., Pauli-blocking. Recently, the importance of light nuclei in supernova matter was also shown by a heavy-ion collision experiment. In the isocaling analysis of Natowitz et al. (2010) the measured symmetry energy can only be explained, if the formation of light nuclei is taken properly into account. Quite remarkably, the deduced temperatures and densities correspond to conditions which are typical for matter in core-collapse supernovae. In the supernova environment light nuclei can possibly influence the neutrino transport and consequently the supernova neutrino signal and dynamics, see, e.g., O’Connor et al. (2007), Arcones et al. (2008), Sumiyoshi & Röpke (2008), and Nakamura et al. (2009). However, so far there are no investigations of core-collapse supernovae, which consistently take into account all light nuclei. With this article we further advance in this direction, by applying the EOS tables of the statistical model of Hempel & Schaffner-Bielich (2010) (HS) to simulations of massive stars.

Statistical models are characterized by having a distribution of nuclei, in which light nuclei can also be

included. On the other hand, the complexity and variety of the involved aspects of nuclear physics require some modeling. Important aspects in the supernova context are for example the interactions of unbound nucleons, excluded volume effects, excited states, Coulomb interactions, nuclear binding energies, shell effects or surface modifications of nuclei, see, e.g., Ishizuka et al. (2003), Botvina & Mishustin (2004), Nadyozhin & Yudin (2004), Nadyozhin & Yudin (2005), Souza et al. (2009), Blinnikov et al. (2011), Hempel & Schaffner-Bielich (2010), Botvina & Mishustin (2010), Arcones et al. (2010), Raduta & Gulminelli (2010), Yudin (2011), and Furusawa et al. (2011). Interestingly, similar statistical models are also used for the analysis of multifragmentation experiments (Koonin & Randrup 1987; Gross 1990; Bondorf et al. 1995). In this article we apply the new EOS from Hempel & Schaffner-Bielich (2010). The HS EOS uses nuclear statistical equilibrium (NSE) with excluded volume effects for distributions of nuclei and RMF interactions of unbound nucleons. In this model all possible light nuclei (e.g., deuterium and tritium) and heavy nuclei up to mass number $A \sim 330$ from the neutron to the proton dripline are included. The knowledge of the detailed composition makes it possible to analyze the impact of different baryon contributions during the different phases of core-collapse supernovae.

The nuclear distributions are especially relevant for weak reactions. For example the new treatments of electron captures on heavy nuclei by Langanke et al. (2003) and Hix et al. (2003) and inelastic neutrino–nucleon (nuclei) scattering by Langanke et al. (2008) are all based on NSE distributions of nuclei. Idealistically, the nuclear physics input in the weak reactions should be as consistent as possible with the EOS and therefore the two parts should be built from the same degrees of freedom. However, also in the present study we use additional simplifications, which will be specified below.

To classify the characteristic features of HS, we take the two aforementioned classic supernova EOS, i.e., LS and STOS, as standard references. These two EOS both use the single nucleus approximation (SNA), i.e., the distribution of heavy nuclei is replaced by a single representative nucleus. Burrows & Lattimer (1984) showed that the SNA has only a minor effect on thermodynamic variables. However, using the SNA instead of nuclear distributions represents a significant difference for the weak reactions, as mentioned already above. Souza et al. (2009) found that the SNA gives also a systematically larger representative heavy nucleus compared to the average of the distribution. There are further limitations of the description of nuclei in the two EOS models: STOS is based on the Thomas–Fermi and local-density approximation and a minimization of the free energy for parameterized nucleon-density profiles within an RMF model. LS is based on a non-relativistic liquid drop description including surface effects. Both models do not include nuclear shell effects and only give an approximate description of the iron-group nuclei, which appear at low temperatures. This leads to artificial shifts in the EOS at the transition to non-NSE. Contrary, due to the use of experimental nuclear masses, the HS model reproduces the thermodynamic state of the ideal gas of, e.g., ^{56}Fe or ^{56}Ni (depending on the proton-to-baryon ratio) at low temperatures by construction and naturally includes

shell effects. Thus, it represents a major improvement to other commonly used EOS as it gives a more detailed description of the chemical composition and the nuclear effects involved at low densities below $\sim 10^{12}$ g/cm³.

However, with statistical models it is difficult to describe the transition to uniform nuclear matter which occurs around half times saturation density, i.e., around 10^{14} g/cm³. Microscopic SNA models allow a more detailed description of the effects which occur at such large densities, like the formation of (non-spherical) inhomogeneous structures, the so-called nuclear pasta phases, see, e.g., Ravenhall et al. (1983) and Newton & Stone (2009). In Hempel & Schaffner-Bielich (2010) it was shown that the thermodynamic variables in the transition region calculated with the HS model are in satisfactory agreement with the results of STOS and LS. From this point of view, the present investigation serves as a practical test whether the HS EOS is suitable to be used for all possible conditions in core-collapse supernova simulations.

Recently, five new supernova EOS tables were calculated with the HS model for different nuclear interactions and are available online.¹ One of the new HS EOS tables is based on the same parameterization TM1 (Sugahara & Toki 1994) of RMF interactions of the nucleons as STOS. This makes it possible to investigate the impact of the model assumptions for the description of inhomogeneous nuclear matter below saturation density, which is one of the main topics of the present study. In addition to TM1 and the general features of the HS model, we also investigate two other RMF parameterizations of nuclear interactions, TMA (Toki et al. (1995)) and FSUgold (Todd-Rutel & Piekarewicz (2005); Piekarewicz (2007)). We note that these two interactions have not been applied in supernova-simulations so far. The different nuclear interactions become significant at high densities and we analyze to which extent they can influence the supernova dynamics and the observable neutrino signal. For the distinction of the different HS EOS we append the used parameterization in brackets, e.g., “HS (TMA)”. To be explicit, sometimes we also use “STOS (TM1)” although the STOS table exists only for TM1. For the LS EOS we append the used incompressibility in brackets, e.g., “LS (180).”

The manuscript is organized as follows. In §2, we present our core-collapse model, including the new HS EOS. The results from simulations of the collapse, bounce, and the early post-bounce phases of a 15 M_⊙ progenitor are presented in §3. We compare HS (TM1) with the LS (180) and the STOS (TM1) EOS and also analyze the neutrino signal. In §4, we discuss the neutrino signal of a 40 M_⊙ progenitor. For this massive progenitor we apply five different EOS: LS (180), LS (220), STOS (TM1), HS (FSUgold), and HS (TMA). We focus on the time until black hole formation, and investigate its relation to characteristic properties of the different nuclear interactions, before we close with a summary in §5.

2. THEORETICAL AND NUMERICAL SETUP

2.1. Core-collapse Supernova Model

Our core-collapse model was originally constructed based on Newtonian radiation hydrodynamics and three

¹ See <http://phys-merger.physik.unibas.ch/~hempel/eos.html>.

TABLE 1
NEUTRINO REACTIONS CONSIDERED, INCLUDING REFERENCES

Weak Process ^a	References
$\nu_e + n \rightleftharpoons p + e^-$	Bruenn (1985)
$\bar{\nu}_e + p \rightleftharpoons n + e^+$	Bruenn (1985)
$\nu_e + \langle A \rangle \rightleftharpoons \langle A \rangle + e^-$	Bruenn (1985)
$\nu + N/\langle A \rangle/\alpha \rightleftharpoons \nu' + N/\langle A \rangle/\alpha$	Bruenn (1985); Mezzacappa & Bruenn (1993a)
$\nu + e^\pm \rightleftharpoons \nu' + e^\pm$	Bruenn (1985); Mezzacappa & Bruenn (1993c)
$\nu + \bar{\nu} \rightleftharpoons e^- + e^+$	Bruenn (1985); Mezzacappa & Messer (1999)
$\nu + \bar{\nu} + N + N \rightleftharpoons N + N$	O. E. B. Messer ^b
$\nu_e + \bar{\nu}_e \rightleftharpoons \nu_{\mu/\tau} + \bar{\nu}_{\mu/\tau}$	Buras et al. (2003); Fischer et al. (2009)

Notes:

^a $\nu = \{\nu_e, \bar{\nu}_e, \nu_{\mu/\tau}, \bar{\nu}_{\mu/\tau}\}$ and $N = \{n, p\}$.

^bPrivate communications, based on Hannestad & Raffelt (1998).

flavor Boltzmann neutrino transport (for details see Mezzacappa & Bruenn 1993a,b,c). It was extended to solve the general relativistic equations for both hydrodynamics and neutrino transport in Liebendörfer et al. (2001), based on the following line-element

$$ds^2 = \alpha^2 dt^2 + \left(\frac{r'}{\Gamma}\right)^2 da^2 + r^2 d\Omega$$

in co-moving coordinates system time t and enclosed baryon mass a , with metric coefficients lapse function $\alpha(t, a)$ and $\Gamma(t, a)$, where $r' = \partial r / \partial a$. $r^2 d\Omega$ describes a 2-sphere, in spherical coordinates (θ, ϕ) , of radius $r(t, a)$. Equations for momentum and energy conservation are obtained via the co-variant derivative of the stress-energy tensor, $\nabla_i T^{ik} = 0$, with

$$T^{tt} = \rho(1 + e + J), \quad T^{aa} = p + \rho K, \quad T^{at} = T^{ta} = \rho H,$$

$$T^{\theta\theta} = T^{\phi\phi} = p + \frac{1}{2}\rho(J - K),$$

where ρ and p are rest-mass density (further discussed below) and matter pressure. e is the specific internal matter energy with respect to the rest-mass density. J and K are the neutrino contributions to the specific internal energy and specific pressure. H is the specific energy exchange between matter and the neutrino radiation field. H , J , and K are the neutrino moments and are given by momentum integrals of the neutrino distribution functions (for details see Liebendörfer et al. 2004). Furthermore, special attention has been devoted to accurately conserve energy, momentum, and lepton number in Liebendörfer et al. (2004).

Neutrino contributions, more precisely the evolution of the neutrino distribution functions f_ν , are computed solving the Boltzmann transport equation for ultrarelativistic and mass-less fermions, for each flavor $\nu = \nu_e, \bar{\nu}_e, \nu_{\mu/\tau}, \bar{\nu}_{\mu/\tau}$. In addition to the space-time coordinates, it depends on the momentum angle θ and energy

E. The left-hand side of the Boltzmann equation determines the phase-space derivative due to transport, and the right-hand side takes collisions into account. The latter relates to the weak processes considered, which are listed in Table 1. Note that for the alpha particles only neutral-current elastic scattering reactions are included. The emission of (μ/τ) -neutrino pairs via the annihilation of trapped $(\nu_e, \bar{\nu}_e)$ has been implemented into our model in Fischer et al. (2009). In the Boltzmann transport representation, for scattering processes we employ reaction kernels, e.g., they take into account final state blocking and depend on incoming and outgoing neutrino angle and energy. For charged-current processes, we employ reaction rates which depend only on the incoming neutrino energy.

The radiation hydrodynamics equations, which are given explicitly in the co-moving frame of reference, are discretized numerically based on a Lagrangian description and an adaptive mesh. They are solved implicitly, where the advection scheme used is second-order total variation diminishing. Details can be obtained in Liebendörfer et al. (2002) and Liebendörfer et al. (2004). For the current study, we include 104 radial adaptive mass zones. Resolution is adapted according to high gradients in density, velocity, and entropy. Furthermore, the outer boundary condition is set by applying a Schwarzschild metric at the outermost mass zone, assuming vacuum outside. In addition, neutrino transport is discretized in 6 angular bins ($\cos\theta \in \{-1, \dots, +1\}$) and 20 energy bins ($E = 3, \dots, 300$ MeV).

In Liebendörfer et al. (2004), the authors compare the model with S. Bruenn’s multi-group flux limited diffusion neutrino transport approximation. A similar comparison with the Boltzmann transport used by the Garching group has been published in Liebendörfer et al. (2005). These two studies show a good qualitative agreement of the spherically symmetric models used by the different groups.

2.2. Use of the EOS

The EOS in supernova simulations is part of the nuclear physics input, next to weak interactions in the neutrino transport. There are two intrinsically different regimes. In NSE, the destruction and production of nuclei is in thermal and chemical equilibrium regarding strong and electromagnetic interactions. The conditions for NSE are achieved typically above a temperature of $T \sim 0.5$ MeV.² For temperatures below $T = 0.44$ MeV, where NSE cannot be applied, we use an ideal Si-gas. For the simulations with the HS and STOS EOS in the non-NSE regime we calculate the baryon EOS as an ideal Maxwell-Boltzmann gas of silicon with the measured nuclear binding energy from Audi et al. (2003). For LS this is not necessary, because the LS routines used in the supernova model also provide the EOS of the silicon gas. The LS routines also handle intrinsically the transition to the NSE regime at temperatures of $T > 0.44$ MeV. For the HS and STOS EOS the baryon component in NSE is given in tabular form. It is a good approximation to treat electrons (and positrons) as a rigid uniform background. Thus they can be added as non-interacting ideal

Fermi-Dirac gases based on Timmes & Arnett (1999). The blackbody contribution of photons is also taken into account.

The baryon EOS tables are stored for given temperature T , baryon number density n_B , and total proton fraction $Y_p = n_p^{\text{tot}}/n_B$. Because of charge neutrality, in the absence of muons the number density of electrons n_e is given by $n_e = Y_p n_B$ which connects the baryon and the electron EOS. Accordingly, Y_p is equivalent to the electron fraction $Y_e = n_e/n_B = Y_p$. All particle densities and fractions used in the article correspond to net densities, i.e., the difference between particle and antiparticle densities, e.g., $n_e = n_{e^-} - n_{e^+}$, $Y_e = Y_{e^-} - Y_{e^+}$. In astrophysics, very often instead of the baryon number density n_B a baryon mass density ρ is used. This is completely equivalent, if ρ is defined as $\rho = n_B m$, with an arbitrary but constant mass m . We will also use such a “baryon mass density” with the usual convention $\rho = n_B m_u$, with the atomic mass unit $m_u = 931.49432$ MeV. However, we want to stress that ρ defined in such a way is not the rest-mass density, because, e.g., the dominant particle species in NSE depends on the thermodynamic state of the system. In a relativistic description of the EOS with interactions there is no conservation of rest mass, but only of the total energy and baryon number. Analogously to the baryon mass density one also defines a baryonic mass $M = N_B m_u$ which is just a redefinition of the total baryon number N_B of the investigated system.

The HS EOS contains the full distribution of all available nuclei, as will be discussed in more detail in the next subsection. However, regarding weak processes we only consider an average heavy nucleus and an average light nucleus. We separate the distribution of all nuclei into light nuclei and heavy nuclei by the charge number six, i.e. carbon:

$$X_a = \sum_{A \geq 2, Z \leq 5} A n_{A,Z} / n_B, \quad (1)$$

$$X_A = \sum_{A \geq 2, Z \geq 6} A n_{A,Z} / n_B, \quad (2)$$

with $n_{A,Z}$ denoting the number density of a nucleus with mass number A and charge number Z , so that the sum of the mass fractions of neutrons X_n , protons X_p , light nuclei X_a and heavy nuclei X_A is unity. The average mass and charge of the light and heavy nuclei are:

$$\langle a \rangle = \sum_{A \geq 2, Z \leq 5} A n_{A,Z} / \sum_{A \geq 2, Z \leq 5} n_{A,Z}, \quad (3)$$

$$\langle z \rangle = \sum_{A \geq 2, Z \leq 5} Z n_{A,Z} / \sum_{A \geq 2, Z \leq 5} n_{A,Z}, \quad (4)$$

$$\langle A \rangle = \sum_{A \geq 2, Z \geq 6} A n_{A,Z} / \sum_{A \geq 2, Z \geq 6} n_{A,Z}, \quad (5)$$

$$\langle Z \rangle = \sum_{A \geq 2, Z \geq 6} Z n_{A,Z} / \sum_{A \geq 2, Z \geq 6} n_{A,Z}. \quad (6)$$

We further simplify the neutrino reactions with light nuclei by treating all of them as alpha particles. Note that for the alpha particles, and thus for all light nuclei, in the present investigation only neutral-current reactions are considered, as listed in Table 1. Charged-

² Throughout the article we use natural units, i.e., $\hbar = c = k_B = 1$, for quantities where it is appropriate.

current and other break-up reactions of the weakly bound light nuclei may also be important in supernova simulations, see, e.g., Nakamura et al. (2009) for neutrino deuteron reactions. However, in this article we first want to investigate their possible appearance and their contribution to the EOS.

2.3. Model of the HS EOS

The HS model consists of an ensemble of nucleons and nuclei in NSE, whereas interactions of the nucleons and excluded volume corrections for the nuclei are implemented. Note that in the present version of the HS EOS tables, the formation of nuclei is neglected for $T > 20$ MeV for simplicity, i.e., matter is assumed to be uniform. At such high temperatures there is only a limited density region slightly below nuclear matter saturation density n_B^0 , where nuclei appear at all. Still it would be better to avoid such a hard switch in the EOS, which we plan to do in future releases of the EOS tables. In the following, we give a brief summary of the HS model, all details can be found in Hempel & Schaffner-Bielich (2010).

For the unbound interacting nucleons (neutrons and protons) an RMF model is applied. Its Lagrangian is based on the exchange of the isoscalar-scalar σ , the isoscalar-vector ω and the isovector-vector ρ mesons between nucleons. In comparison with more sophisticated theoretical approaches, based on nucleon-nucleon scattering data, it has been recognized that nonlinear σ and ω self-coupling terms are necessary to achieve a reasonable description of the EOS at high densities and the properties of nuclei at the same time, see, e.g., Sugahara & Toki (1994). An alternative approach, which is not used in the present investigation, is RMF models with density-dependent couplings, see, e.g., Typel (2005). The free parameters of the Lagrangians, the meson masses and their coupling strengths, have to be determined by fits to experimental data.

We apply three different RMF parameterizations: TM1 by Sugahara & Toki (1994), TMA by Toki et al. (1995), and FSUgold by Todd-Rutel & Piekarewicz (2005). The Lagrangians of TM1 and TMA have the same form and include nonlinear terms of the σ and ω mesons. TM1 was developed together with TM2, which were fitted to binding energies and charge radii of light (TM2) and heavy nuclei (TM1). TMA is based on an interpolation of these two parameter sets. The coupling parameters g_i of the set TMA are chosen to be mass-number dependent of the form $g_i = a_i + b_i/A^{0.4}$, with a_i and b_i being constants, to have a good description of nuclei over the entire range of mass numbers. For uniform nuclear matter the couplings become constants and are given by a_i . TMA was also used in Hempel & Schaffner-Bielich (2010), where the HS model was introduced. FSUgold includes the coupling between the ω and the ρ meson in addition. This leads to a better description of nuclear collective modes, the EOS of asymmetric nuclear matter and a different density dependence of the symmetry energy (Piekarewicz 2007) which is very low at large densities. The coupling constants of FSUgold are fitted to binding energies and charge radii of a selection of magic nuclei.

The HS EOS tables take into account the experimental data on nuclear masses from Audi et al. (2003). For

the masses of the experimentally unknown nuclei different theoretical nuclear structure calculations in form of nuclear mass tables are used. The TMA interactions are combined with the mass table of Geng et al. (2005), which is also calculated with the RMF model TMA. Thus all nuclear interactions are consistent. This mass table lists 6969 even-even, even-odd, and odd-odd nuclei, extending from ${}^{16}_8\text{O}$ to ${}^{331}_{100}\text{Fm}$ from slightly above the proton to slightly below the neutron drip line. The nuclear binding energies are calculated under consideration of axial deformations and the pairing is included with a BCS-type δ -force. For the parameterization TM1 we do not have a suitable mass table at hand, thus we cannot avoid the minor inconsistency to also use the table of Geng et al. (2005), which is based on the TMA parameterization. For FSUgold we take a mass table calculated by X. Roca-Maza, which was previously applied for the outer crust of neutron stars (Roca-Maza & Piekarewicz 2008). This table contains 1512 even-even nuclei, from the proton to the neutron drip, with $14 \leq A \leq 348$ and $8 \leq Z \leq 100$. Odd nuclei are not included in this table. The nuclei were calculated only with spherical symmetry and the pairing is introduced through a BCS approach with constant matrix elements. The constant matrix element for neutrons has been fitted to reproduce the experimental binding in the tin isotopic chain and the constant matrix element for protons to the experimental binding in the $N = 82$ isotonic chain.

To describe nuclei in the supernova environment, we not only need binding energies, but have to account for medium and temperature effects. For the screening of the Coulomb field of nuclei in the uniform background of electrons we use the most basic expression: for each nucleus we assume a spherical Wigner-Seitz (WS) cell at zero temperature. More elaborated approaches for the Coulomb energy of a multi-component plasma at finite temperature can, e.g., be found in Nadyozhin & Yudin (2005), Potekhin et al. (2009), and Potekhin & Chabrier (2010). However, we leave this for future studies as the Coulomb energy becomes only important at low temperatures so that the simplest expression is sufficient for our purposes.

Finite temperature leads to the population of excited states of nuclei. Here, we use the temperature dependent degeneracy function of Fái & Randrup (1982). It is the same analytic expression as in the original reference of the HS model (Hempel & Schaffner-Bielich 2010) and used previously by Ishizuka et al. (2003), but now we consider only excitation energies below the binding energy of the corresponding nucleus, in order to represent that the excited states still have to be bound (see, e.g., Röpke (1984)). We note that the inclusion of excited states up to infinite energies had only a minor influence on the composition but would lead to an unphysically large contribution of the excited states to the energy density and entropy at very high temperatures.

We describe nuclear matter as a chemical mixture of the different nuclear species and nucleons. As we distinguish between nuclei and the surrounding interacting nucleons we still have to specify how the system is composed of the different particles. Our thermodynamic model is built on two main assumptions: first, we assume for unbound nucleons that they are not allowed to be situated inside of nuclei, whereas nuclei are described as uniform

hard spheres at saturation density n_B^0 . Second, for nuclei (with mass number $A \geq 2$) we assume that they must not overlap with any other baryon in the system (nuclei or unbound nucleons). Thus, we take the volume which is available for the nucleons to be the part of the total volume of the system which is not excluded by nuclei. This is described by the filling factor of the nucleons

$$\xi = 1 - \sum_{A,Z} A n_{A,Z} / n_B^0 \quad (7)$$

(here and in the following, we refer to $A \geq 2$). The free volume in which a nucleus can move is the total volume minus the volume filled by nuclei and nucleons. This is incorporated via the free volume fraction

$$\kappa = 1 - n_B / n_B^0, \quad (8)$$

with the total baryon number density n_B , which includes contributions from unbound neutrons and protons:

$$n_B = n_n + n_p + \sum_{A,Z} A n_{A,Z}. \quad (9)$$

Based on these two main assumptions, the EOS is derived in a consistent way, using the non-relativistic Maxwell–Boltzmann description for nuclei and the full Fermi–Dirac integrals for nucleons (solved with the routines from Aparicio (1998) and Gong et al. (2001)). We obtain modifications of all thermodynamic quantities due to the excluded volume, in agreement with the results of Yudin (2011) who studied excluded-volume schemes in general. Here we give the thermodynamic potential, the free energy density f , as an example:

$$f = \sum_{A,Z} f_{A,Z}^0(T, n_{A,Z}) + \sum_{A,Z} f_{A,Z}^{\text{Coul}} - T \sum_{A,Z} n_{A,Z} \ln(\kappa) + \xi f_{\text{RMF}}^0(T, n_n/\xi, n_p/\xi). \quad (10)$$

The first term in Eq. (10) is the summed ideal gas expression of nuclei. The Coulomb free energy of nuclei appears in addition. The third term is the direct contribution from the excluded volume. Because of this term, as long as nuclei are present, the free energy density goes to infinity when approaching saturation density, because the free volume of nuclei goes to zero, $\kappa \rightarrow 0$. Thus, nuclei will always disappear before saturation density is reached. The RMF contribution of the nucleons, f_{RMF}^0 , is weighted with their filling factor ξ , as the free energy is an extensive quantity. If nuclei are absent, $\xi = 1$, and we get the unmodified RMF description, as it should be. The excluded volume correction for the nuclei represents a hard-core repulsion of the nuclei at high densities close to saturation density. Instead the modification of the free energy of the unbound nucleons is purely geometric and just describes that the nucleons fill only a fraction of the total volume. In this sense, the two aforementioned model assumptions for the excluded volume are essential, as they lead to the desired limiting behavior of the EOS.

2.4. EOS Characteristics and Constraints

Table 2 lists some characteristic saturation properties of uniform bulk nuclear matter for the three different RMF parameterizations. We also include results for the

TABLE 2
PROPERTIES AT SATURATION DENSITY OF THE DIFFERENT EOS
UNDER INVESTIGATION

EOS	n_B^0 [fm $^{-3}$]	E_0 [MeV]	K [MeV]	K' [MeV]	J [MeV]	L [MeV]
TM1	0.145	16.3	281	-285	36.9	111
TMA	0.147	16.0	318	-572	30.7	90
FSUgold	0.148	16.3	230	-524	32.6	60
LS (180)	0.155	16.0	180	-451	28.6	74
LS (220)	0.155	16.0	220	-411	28.6	74

Note. Definition of the quantities given in the text.

LS EOS with the incompressibilities of $K = 180$ and 220 MeV. The quantities shown in Table 2 correspond to the coefficients of the following power-series expansion of the binding energy per baryon at $T = 0$ around the saturation point:

$$E(x, \beta) = -E_0 + \frac{1}{18} K x^2 + \frac{1}{162} K' x^3 + \dots + \beta^2 \left(J + \frac{1}{3} L x + \dots \right) + \dots, \quad (11)$$

with $x = n_B / n_B^0 - 1$ denoting the relative deviation from the saturation density, and the asymmetry parameter β which is given by the total proton fraction: $\beta = 1 - 2Y_p$. Next we discuss the listed nuclear matter properties briefly and compare with experimental constraints. The saturation point itself, i.e., the saturation density n_B^0 and the corresponding binding energy per nucleon E_0 , can be determined from the analysis of nuclear binding energies. All EOS models give reasonable values for n_B^0 and E_0 . The nuclear incompressibility K can be studied experimentally, e.g., by exciting the isoscalar giant monopole resonance (ISGMR), leading to values of $K = 240 \pm 10$ MeV (Piekarewicz 2010). FSUgold and LS (220) agree roughly with this experimental constraint, TM1 is still reasonable, but the value of TMA is too large and the value of LS (180) too low. However, it is perceived in the literature that the extraction of K from ISGMR data is not unambiguous. The experiments probe nuclear matter slightly below saturation density and furthermore the deduced results depend on the nuclear interactions (e.g., the behavior of the symmetry energy) which are taken for the data analysis (see, e.g., Shlomo et al. (2006); Piekarewicz (2004); Sharma (2009)). One also still has difficulties to explain all available ISGMR data consistently with a single theoretical model (Piekarewicz 2010). The skewness coefficient K' is the third-order term for the expansion of the energy per nucleon around n_B^0 and is not constrained directly by experiments so far. Still there exist some estimates: based on a correlation study of Skyrme–Hartree–Fock models, Chen (2012) deduces $K' = -355 \pm 95$ MeV. Only TM1 and LS (220) lie within this region.

Typical values for the symmetry energy coefficient J range from 28 to 34 MeV, whereas most studies give mean values around 32 MeV, see, e.g., Tsang et al. (2009). Thus the symmetry energy of TM1 does not comply with the experimental results, but all other EOS do. We remark that the values of J shown for LS, which we calculated with the numerical routines which are available online, agree only approximately with the value

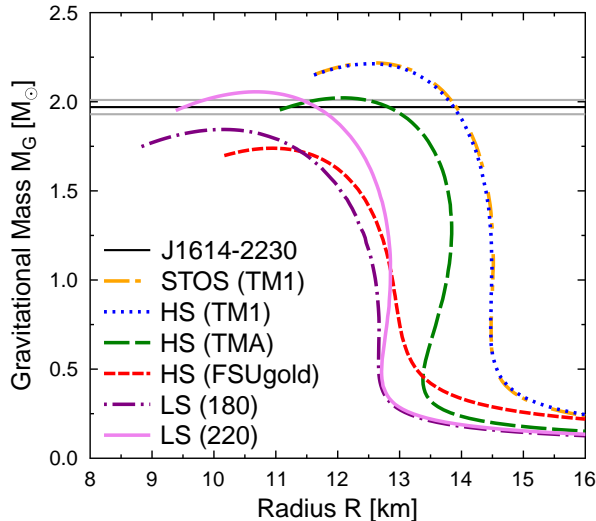


FIG. 1.— Mass–radius relation of cold neutron stars for the EOS under investigation. The gray and black horizontal lines show the measurement of the mass of the pulsar PSR J1614-2230 with its 1σ error (Demorest et al. 2010).

given in the original work by Lattimer & Swesty (1991) of $J = 29.3$ MeV. The slope of the symmetry energy, L , shows an important correlation with the neutron skin thickness of heavy nuclei (Roca-Maza et al. 2011) which is currently being measured by the PREX experiment at JLAB. Interestingly, L is also correlated with the radii of neutron stars (Horowitz & Piekarewicz 2001). There are various experimental probes for L , leading to constraints ranging from 40 to 110 MeV with a common center around 75 MeV, see the comprehensive compilations of Carbone et al. (2010) and Tsang et al. (2009). In some nuclear models a large value of J is compensated by a large value of L in the fitting procedure of the free parameters, to achieve a similar symmetry energy slightly below saturation density. This is also seen for TM1, which gives too large values of J and L . The other investigated EOS give reasonable results for L .

We want to emphasize the following, simple point which will reappear several times during the later discussion of our results: single parameters do not characterize the global behavior of the EOS. To give one example, one could think that TM1 is softer than TMA because of the lower incompressibility. However, the slight change of the saturation point and less negative higher order terms such as the skewness coefficient in TM1 lead to the unexpected result that the pressure of symmetric nuclear matter in TM1 is always larger than in TMA, i.e., TM1 is stiffer. Furthermore, for supernovae and neutron stars the symmetry energy plays an important role. The extremely large symmetry energy of TM1 stiffens its neutron star EOS additionally. Thus for TM1 one obtains a maximum mass of cold neutron stars, which is significantly larger than the one of TMA, as we will see next.

In 2010, the gravitational mass of the millisecond pulsar PSR J1614-2230 was determined to be $M_G = 1.97 \pm 0.04 M_\odot$ by measuring the Shapiro delay (Demorest et al. 2010). It represents the largest robust maximum mass measurement at present and thus the most important constraint for the mass–radius relations of neutron stars. In Fig. 1, we show this constraint with its 1σ error to-

gether with the mass–radius relations of the EOS which are investigated in this article. The curves have been calculated with the tables which are used in the simulations presented below by imposing beta-equilibrium without neutrinos at practically zero temperature, i.e., $T = 0.1$ MeV, and solving the Tolman–Oppenheimer–Volkoff equations. The values of the corresponding maximum masses of neutron stars are $2.219 M_\odot$, $2.213 M_\odot$, $2.022 M_\odot$, $1.739 M_\odot$, $1.844 M_\odot$, and $2.056 M_\odot$ for STOS (TM1), HS (TM1), HS (TMA), HS (FSUgold), LS (180), and LS (220), respectively. The mass–radius curves of STOS (TM1) and HS (TM1) are almost identical, because they are built with the same RMF parameterization TM1. This good agreement shows that there are only small differences in the pressure–energy density relation between the two EOS models, despite the different description of non-uniform nuclear matter. FSUgold and LS (180) fail to fulfill the constraint of PSR J1614-2230. Despite this, we include FSUgold in the present study, to explore the implications of a very soft RMF EOS and because of its good description of low-density nuclear matter. We also keep LS (180), because it is a standard reference for core-collapse supernova simulations. The stiff TM1 parameterization lies well above the maximum mass constraint, whereas TMA and LS (220) are only slightly above.

Steiner et al. (2010) used observational data of masses and radii of seven neutron stars with well-determined distances in a Bayesian framework to determine nuclear matter parameters and the neutron star EOS. The found values for the saturation properties of nuclear matter agree remarkably well with the aforementioned experimental constraints. Furthermore, the authors deduce a mass–radius relation which is based on the analysis of the observational data and find relatively small neutron star radii around 11 to 12 km for $M_G = 1.4 M_\odot$, indicating a soft behavior of the neutron star EOS around saturation density. Only LS (180) is compatible with such small radii, and FSUgold and LS (220) come close to it. The radii of TMA and TM1 seem to be much too large.

We conclude that TMA has satisfying nuclear matter properties, apart from the too large value of the incompressibility. For TM1 the incompressibility is barely acceptable, but the symmetry energy and its slope are too large. On the other hand, these two EOS are not compatible with small neutron star radii found by Steiner et al. (2010). FSUgold has very nice nuclear matter properties and a lot of success in nuclear structure, but unfortunately it gives a too low maximum mass. Also LS (180) with an incompressibility of 180 MeV is actually ruled out by the observation of PSR J1614-2230, and furthermore its incompressibility and symmetry energy are too low. LS (220) gives satisfactory results. It would be good if other new EOS tables became available in the future which comply better with all the experimental and observational results. The emphasis of the present study is a different one. We want to explore a broad range of possible EOS, including extreme cases, to better understand the impact of the EOS in core-collapse supernovae.

3. RESULTS: GENERAL FEATURES OF THE HS EOS

In the following subsections, we will compare the HS EOS with the parameterization TM1 (HS (TM1)),

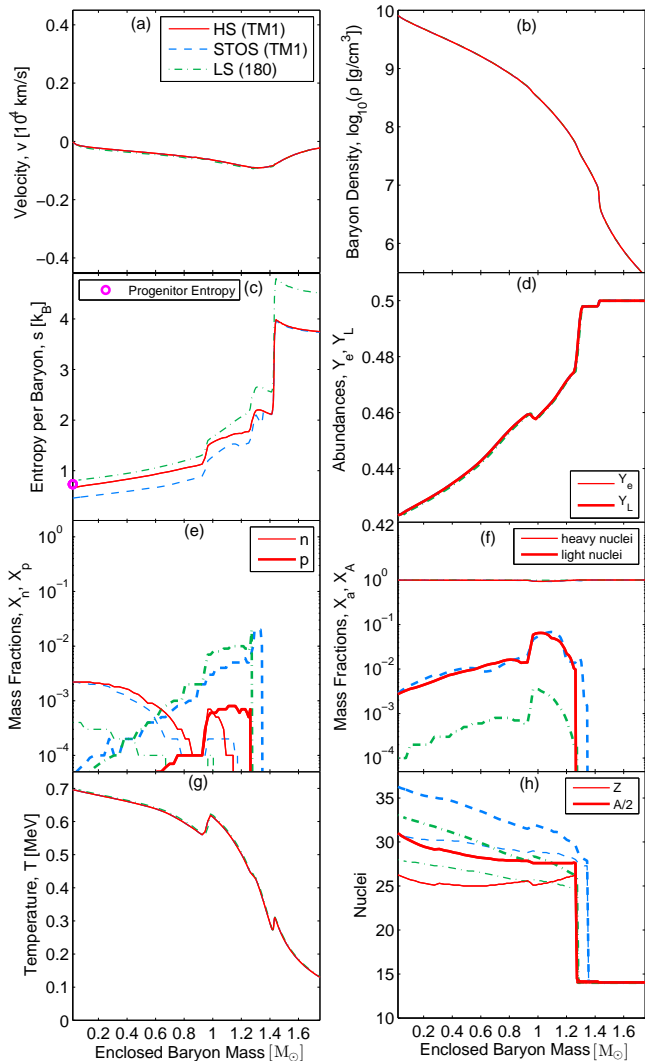


FIG. 2.— Radial profiles of selected hydrodynamic quantities with respect to the enclosed baryon mass for the $15 M_{\odot}$ progenitor model from Woosley and Weaver (1995) at the progenitor stage, comparing the different EOS of HS (TM1) (red solid lines), STOS (TM1) (blue dashed lines) and LS (180) (green dash-dotted lines). In panel (d), Y_e is the electron fraction, and Y_L the electron lepton fraction. “light nuclei” in panel (f) corresponds to the mass fraction of alpha particles for STOS and LS, and the mass fraction X_a of light nuclei with $Z \leq 5$ for HS. “heavy nuclei” is the mass fraction of the representative heavy nucleus for STOS and LS, and the mass fraction X_A of all nuclei with $Z \geq 6$ in HS. Panel (h) shows the charge and mass number of the representative heavy nucleus for STOS and LS, respectively, the average charge and mass number of the distribution of heavy nuclei for HS. See the text for further details.

introduced in § 2, with the standard EOS from Lattimer & Swesty (1991) with an incompressibility of 180 MeV (LS (180)) as well as H. Shen et al. (1998a) (STOS (TM1)). Note that STOS is also based on the TM1 parameterization. We examine the collapse, bounce and early post-bounce phases at the example of the $15 M_{\odot}$ progenitor model from Woosley and Weaver (1995). In this section, we do not consider the LS (220) EOS or any of the other RMF parameterizations of the HS EOS. Thus in the following discussion sometimes we omit the specification “(180)” for the “LS (180)” EOS. The same holds for the “HS (TM1)” and “STOS (TM1)”

EOS, where we sometimes use only “HS” or “STOS” for simplicity.

3.1. Progenitor Stage

The differences between the EOS can already be identified at the progenitor stage, illustrated via radial profiles in Fig. 2 for the $15 M_{\odot}$ progenitor of Woosley and Weaver (1995). We note that we take the temperature, density, and electron fraction from the progenitor as the initial configuration for the core-collapse simulation, that is why these quantities are the same for all three EOS. For the part of the contracting progenitor star which is shown in Fig. 2, the baryon density ranges from 10^{10} to 10^5 g/cm³ and the entropy per baryon from 0.5 to 5 k_B , corresponding to temperatures of 0.7–0.1 MeV. Matter at the center is already slightly asymmetric, whereas the electron fraction ranges from $Y_e \sim 0.42$ at the very center to 0.5 at the lowest densities shown in the figure. Note that the electron lepton fraction $Y_L = Y_{\nu_e} + Y_e$, with the net electron-flavor neutrino fraction Y_{ν_e} , is on top of the electron fraction, as the abundance of electron neutrinos (and all other neutrinos, too) is still negligible. One sees that the composition is dominated by heavy nuclei, only at a region around $M_B \sim 1 M_{\odot}$ alpha particles contribute with up to 10 % to the mass fraction.

Next we compare the state of the progenitor described by the three EOS in detail. We note that the HS EOS should give the most accurate description of the progenitor stage, as it includes shell effects and experimentally measured binding energies. Medium modifications of the properties of nuclei are negligible at such low densities and temperatures encountered here. The fraction of light nuclei X_a with $Z \leq 5$ in the HS EOS is almost identical to the alpha-particle fraction of STOS, showing that the additional light nuclei are negligible at the progenitor stage. LS gives a reduction of the alpha-particle fraction of almost one order of magnitude, which can be attributed to a well-known error in the alpha-particle binding energy in the LS routines (Swesty & Myra 2005). In the reference simulations which we show here, we did not correct for this error. Apart from this difference, the dependence of the alpha-particle abundance on density is very similar in the three EOS.

The fraction of unbound nucleons is much more model dependent, due to the interplay between unbound nucleons and the formation of heavy nuclei. Regarding heavy nuclei in the inner layers, there is a clear tendency of STOS to give the largest mass numbers, followed by LS and HS with the smallest heavy nuclei. As expected from stellar nucleosynthesis, iron-group nuclei are found in HS. In contrast, STOS gives nuclei around $Z \sim 30$. Compared to the composition of the progenitor (not shown in Fig. 2, because only limited information was available), all EOS show some significant differences, because NSE has actually not been reached completely in the progenitor calculation, even though temperatures are above 0.5 MeV. For example, there is still up to 20 % of carbon in the very center. Also thermodynamic quantities are affected from the fact that the progenitor is not in full NSE. For example, the central entropy per baryon of the progenitor model (purple circle in Fig. 2(c)) is slightly larger than in HS, because the average mass number of heavy nuclei is lower than the value obtained from NSE. LS

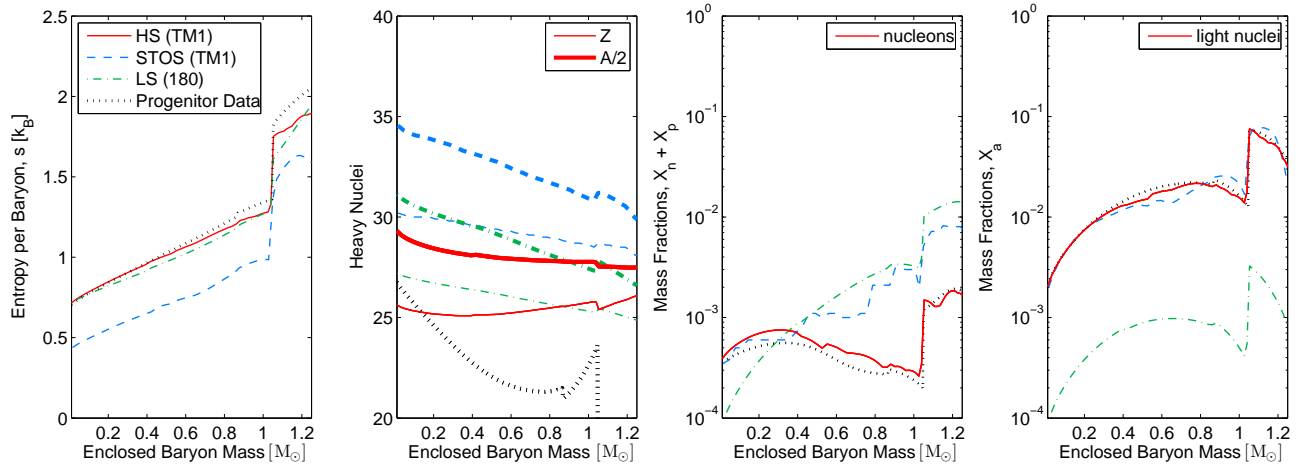


FIG. 3.— Radial profiles of the entropy per baryon and the nuclear composition for the $15 M_{\odot}$ progenitor model from Woosley et al. (2002) at the progenitor stage, with the same notation as in Fig. 2. In addition, we also compare with the progenitor data (black dotted lines) given by the stellar evolution calculation. Note that only the average mass number, but not the charge number of heavy nuclei, was available in the progenitor data and is depicted in the figure.

gives a similar but a bit larger entropy than HS. In contrast, the entropy of STOS is significantly lower, which we will explain in the discussion of the $15 M_{\odot}$ progenitor of Woosley et al. (2002) shown in Fig. 3.

We discuss this progenitor too, because the available data include entropy profiles and more detailed information about the nuclear composition. Furthermore, this progenitor is closer to NSE than the one of Woosley and Weaver (1995) shown before. Regarding the composition, similar trends of the three EOS as in Fig. 2 are observed. In comparison with the original progenitor data, there is a perfect agreement with HS for the mass fractions of the different particles. However, the average mass number of heavy nuclei from the progenitor calculation is still below the NSE value from HS. HS and LS reproduce the entropy profile of the progenitor very well, but the entropy per baryon of STOS is almost $0.3 k_B$ lower. For the shown conditions, the entropy is mainly given by heavy nuclei. The entropy of heavy nuclei can be split in two contributions: internal excitations and kinetic entropy from the thermal movement of nuclei. All three EOS take into account internal excitations of nuclei, but describe it in different ways. Furthermore, only HS has a distribution of nuclei, whereas STOS and LS are based on the SNA. However, the largely reduced entropy of STOS is mainly due to the absence of the kinetic entropy of nuclei. The nuclear kinetic entropy per baryon is on the order of $0.2 k_B$ in LS and HS, which explains the reduction of the entropy in STOS seen in Figs. 2 and 3. This means that STOS assumes always a lattice of nuclei, even if a crystal would actually form only at lower temperatures. Also the energy density, the pressure, and the chemical potentials of STOS lack in the kinetic contribution of nuclei in the ideal gas regime at low densities and moderate temperatures. This is a typical problem of SNA models. LS resolves this problem by adding an explicit kinetic contribution of heavy nuclei to the free energy.

3.2. Core Collapse and Bounce

To follow the evolution of the core-collapse phase, in Fig. 4, we show radial profiles of selected quanti-

ties for the three EOS under investigation (LS (180), STOS (TM1), HS (TM1)), when the central temperatures reach ~ 1 MeV. The selected states correspond to slightly different times in the simulation around 40 ms before bounce, but represent similar stages of the evolution. For the collapse phase until the stage shown in Fig. 4, the evolution of the inner core proceeded homogeneously. No shock has formed and any possible change of the entropy per baryon is given only by weak reactions. As long as the densities are low, neutrinos emitted can leave without interactions. As explained in Bruenn (1985) and Liebendörfer (2005), during the early stage of collapse the entropy generation by electron captures is roughly balanced by the entropy carried away by neutrinos. Here, we also find that the entropy profiles remain almost unchanged. However, a large difference of the entropy per baryon developed at $\sim 1.4 M_{\odot}$ between the three EOS, which relates to the different transitions from non-NSE to NSE. The huge difference between LS and the other two EOS is caused by the different non-NSE treatment for LS mentioned in § 2.2. It is to some extent artificial and can be safely ignored. Due to the ongoing compression, the matter in the entire collapsing core is heated slightly, which in turn increases the fraction of alpha particles and nucleons by almost one order of magnitude. By comparing the average mass and charge numbers of heavy nuclei, one sees that some electron captures have taken place, and that the mass numbers have been increased. These processes and the evolution occur in an overall similar manner for the three different EOS. The differences which were observed for the progenitor in Fig. 2, i.e., larger nuclei in STOS and LS, different nucleon fractions, and a too low entropy in STOS, can still be identified.

However, some quantities which were identical at the progenitor stage developed differently. Let us focus on the comparison of HS (TM1) and STOS (TM1) which are built from the same nuclear interactions. For example, the electron fraction shows an interesting evolution. Up to $0.4 M_{\odot}$, HS leads to a faster deleptonization than STOS. We explain this by the used prescription of electron captures on heavy nuclei by Bruenn (1985),

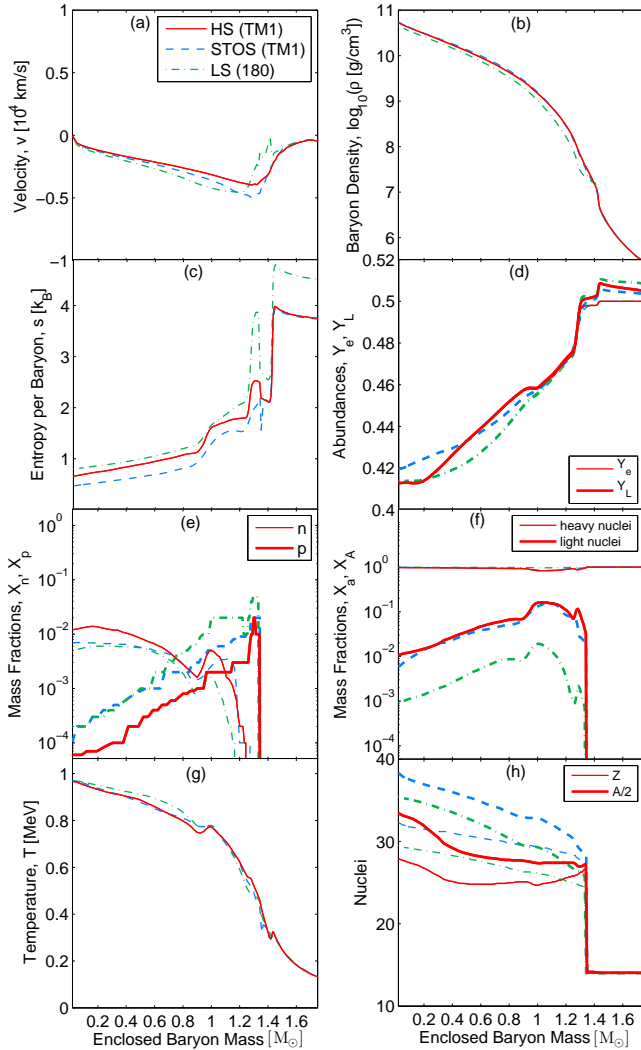


FIG. 4.— Radial profiles of selected hydrodynamic quantities with respect to the enclosed baryon mass during the core-collapse phase for the $15 M_{\odot}$ progenitor model from Woosley and Weaver (1995), when the central temperature $T_{\text{central}} \simeq 1$ MeV. Shown are the HS (TM1) EOS at $t_{\text{pb}} = -42.9$ ms (red solid lines), the STOS (TM1) EOS at $t_{\text{pb}} = -42.1$ ms (blue dashed lines), and the LS (180) EOS at $t_{\text{pb}} = -39.1$ ms (green dash-dotted lines). The notation is the same as in Fig. 2.

where the rate decreases with the excess neutrons of a nucleus. Even though $\langle Z \rangle / \langle A \rangle$ is roughly the same in HS and STOS, because nuclei in STOS are significantly larger, the number of excess neutrons is larger, leading to smaller electron-capture rates. We leave the question whether this effect would persist in the more elaborated descriptions of electron capture on heavy nuclei of Hix et al. (2003) and Langanke et al. (2003) for future studies. Between $0.4 M_{\odot} < M_B < 1 M_{\odot}$, the deleptonization was slower in HS than in STOS. This is the domain which is dominated by electron captures on free protons. Because the free-proton fraction is larger in STOS than in HS (see Fig. 4(e)) electron captures in STOS are faster. Because the electron contribution to the EOS is dominating in this region, the smaller electron fraction of STOS still has a small effect on hydrodynamic variables like the infall velocity or the baryon density, which are slightly increased in STOS.

Figure 5 shows the evolution of the collapse when the central temperatures reach roughly 5 MeV corresponding to ~ 0.1 ms before bounce. By comparing the fraction of light nuclei X_a of HS with the alpha-particle fraction of STOS in Figs. 4 and 5 (thick lines in graphs (f)) one realizes that other light nuclei than alpha particles have been formed with HS in the center during these two stages of the collapsing star. The total fraction of light nuclei in the center is almost 10% in Fig. 5, whereas the alpha particle fraction has decreased below 1%. If weak processes with the additional light nuclei were taken into account, in principle this could also modify the neutrino transport and deleptonization. However, the fraction of light nuclei other than alpha particles starts to rise only shortly before the stage shown in Fig. 5. For example, the fraction of ${}^3\text{H}$ gets larger than the alpha-particle fraction around 2 ms before bounce. At this stage, neutrinos are already trapped in the center. Thus we expect that the additional light nuclei have only little influence on the deleptonization.

At the stage of Fig. 5 there is a significant number of trapped neutrinos. At the center of the star the electron and lepton fractions in HS are still lower than in STOS. The change of the electron fraction at the center during the stages of Fig. 4 and Fig. 5, i.e., the number of electron captures is very similar for the two EOS: $\Delta Y_e^{\text{HS}} = -0.1261$ and $\Delta Y_e^{\text{STOS}} = -0.1222$. Also the change of the central lepton fraction was similar for the two EOS, they give a similar amount of deleptonization in the center. In the outer layers the differences in the lepton fraction profiles are less pronounced and it appears that STOS and LS are closer to each other than STOS and HS. Interestingly, the electron and lepton fraction profiles show a more step-like change in HS. These steps coincide with larger changes of the average mass and charge number of heavy nuclei which are caused by neutron magic shell effects, as will be further illustrated below.

In the profiles of the entropy per baryon an increase of $\sim 0.5 k_B$ is observed in the center. The entropy creation occurs between the two stages of Figs. 4 and 5, before neutrinos become trapped and reach weak equilibrium. This happens at the stage where the entropy loss by neutrino transport is smaller than the entropy gain from local weak reactions. If we compare the entropy profiles of HS and STOS we see that the difference of the entropy per baryon for $M_B > 0.6 M_{\odot}$ is the same as it was at the progenitor stage. Contrary, in Fig. 5 at the center, HS and STOS have equal entropies per baryon, thus there was a larger entropy production in STOS of $\Delta s^{\text{STOS}} \sim 0.65 k_B$ than in HS of $\Delta s^{\text{HS}} \sim 0.47 k_B$. Where does this additional entropy come from? Based on the work of Bruenn (1985), Liebendörfer (2005) showed that the entropy production can be well approximated by

$$T ds = -dY_e (\Delta\mu - E_{\nu}^{\text{esc}}), \quad (12)$$

$$\Delta\mu = \mu_e + \mu_p - \mu_n, \quad (13)$$

where E_{ν}^{esc} denotes the typical energy of escaping neutrinos which is on the order of 10 MeV, and $\Delta\mu > 0$ is the average chemical energy which is liberated by an electron capture. μ_e , μ_p , and μ_n are the relativistic chemical potentials of electrons, protons, and neutrons, i.e., they include the corresponding rest masses. Note that

neutrinos are emitted at a lower energy than they are produced, because they thermalize by inelastic scattering before escape. As the change of the electron fraction, the electron neutrino luminosities and the temperature evolution are very similar in HS and STOS, we find that the difference of the change of the entropy per baryon, $\Delta s^{\text{STOS}} - \Delta s^{\text{HS}} \sim 0.2 k_B$, has to originate from a difference $\Delta\mu^{\text{STOS}} - \Delta\mu^{\text{HS}}$ on the order of several MeV. This means that electron captures in STOS give a larger release of entropy than in HS. Indeed, by carefully comparing the chemical potentials of HS and STOS (see Hempel & Schaffner-Bielich (2010)) one finds that the non-relativistic proton chemical potentials (i.e., without the proton rest mass) for the conditions encountered here are slightly lower in HS than in STOS. This is due to the different description of non-uniform matter and nuclei. Also light nuclei other than alpha particles, which form during the two stages of the collapsing star shown in Figs. 4 and 5 (graphs (f)), give a small modification of the chemical potentials in HS. On the other hand, STOS has in general larger electron fractions in the center, so that μ_e will be larger, leading to an increase of $\Delta\mu^{\text{STOS}}$ compared to $\Delta\mu^{\text{HS}}$. This means that electron captures are more energetic, because matter in STOS is still more symmetric than in HS.

Furthermore, the nucleon rest masses employed in the EOS have an interesting effect on the entropy production as we will discuss now. The EOS model of STOS does not include the neutron-to-proton rest-mass difference, but only a common nucleon mass of 938 MeV. Contrary, HS is built on the measured neutron and proton masses. For the conditions encountered here, the nucleon rest masses contribute directly to the energy and free energy densities and the relativistic chemical potentials. Thus, the rest-mass difference is included in $\Delta\mu^{\text{HS}}$ but not in $\Delta\mu^{\text{STOS}}$, which alone changes $\Delta\mu$ already by $\Delta m \sim 1.2935$ MeV. We conclude, that the appearance of light nuclei, the faster deleptonization in the early phases of the collapse and realistic nucleon masses lead to less entropy gain for electron captures in HS.

We want to emphasize that in the electron/positron capture rates based on Bruenn (1985) which determine dY_e , the nucleon rest-mass difference Δm is taken into account, independent of the EOS. This is done by using the chemical potentials without rest mass and explicitly adding Δm to the Q -value. Thus, in both simulations the energy of the produced neutrinos and the rate of deleptonization is determined correctly taking into account the rest-mass difference of the nucleons. The missing rest-mass difference in STOS leads only to a slight overestimation of the entropy production, as discussed before. This also explains why the change of the electron fraction is so similar for the two EOS, despite the different entropy production. In this context we also want to remark that the nucleon rest masses have only a negligible effect on the equilibrium (NSE) composition, as long as the same rest masses are used for all nucleons, i.e., for free nucleons and nucleons bound in nuclei.

Let us turn to the temperature evolution. In Fig. 4, the central temperature was equal for STOS and HS. Now the temperature of STOS has increased to larger values than in HS which is in agreement with the larger entropy increase in STOS. However, one also has to note that the densities reached in HS are slightly smaller than in

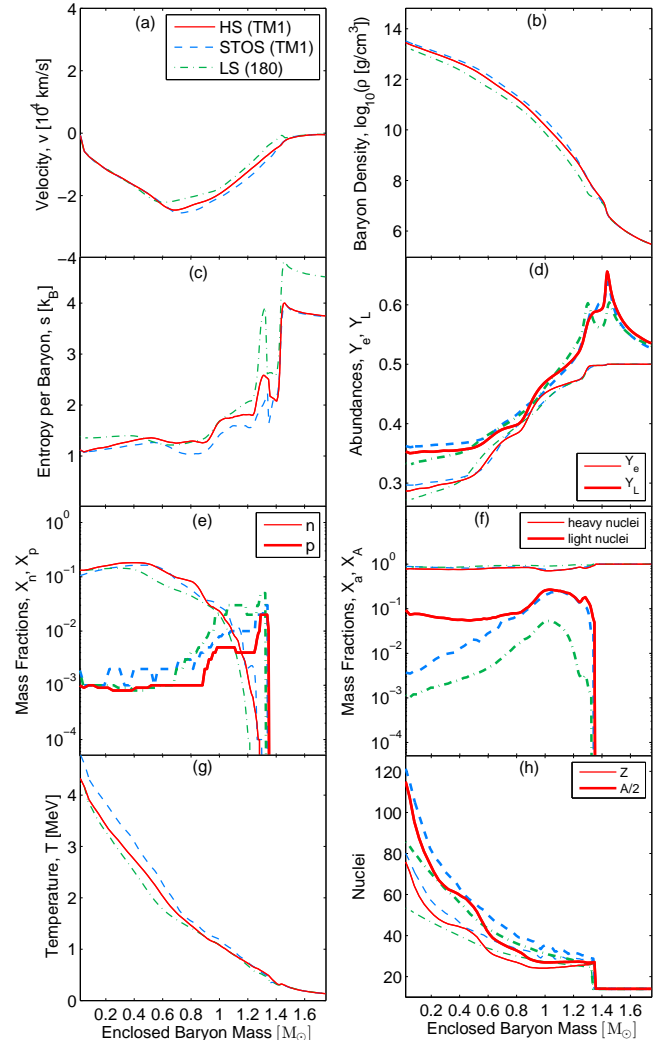


FIG. 5.— Same as Fig. 4 but at $T_{\text{central}} \simeq 5$ MeV. The states correspond to $t_{\text{pb}} = -0.91$ ms for HS (TM1), $t_{\text{pb}} = -0.84$ ms for STOS (TM1), and $t_{\text{pb}} = -1.09$ ms for LS (180).

STOS, so there is less compression heating. In this context we have to remark that minor differences can also be due to the different data sampling, because profiles which are shown in the same figure can correspond to slightly different evolutionary states. However, we checked that the differences which we see and which we discuss here are systematic and not caused by the different data sampling.

Less than 1 ms later, the core bounce takes place, which is depicted in Fig. 6. It is defined as the moment when the maximum central density is obtained at the end of the iron-core collapse. Regarding the Y_e and entropy profiles we can identify the same differences between HS and STOS as described before. From Fig. 6 we can see that the shock is located at a slightly lower mass in HS. It is well known that the mass of the inner core is proportional to Y_e^2 (see Goldreich & Weber 1980; Martínez-Pinedo et al. 2006), which explains this result to some extent. During the collapse evolution the temperature of HS was similar to the one of STOS. Now at bounce we see that the core temperature of HS has become larger than in STOS. It can also be attributed

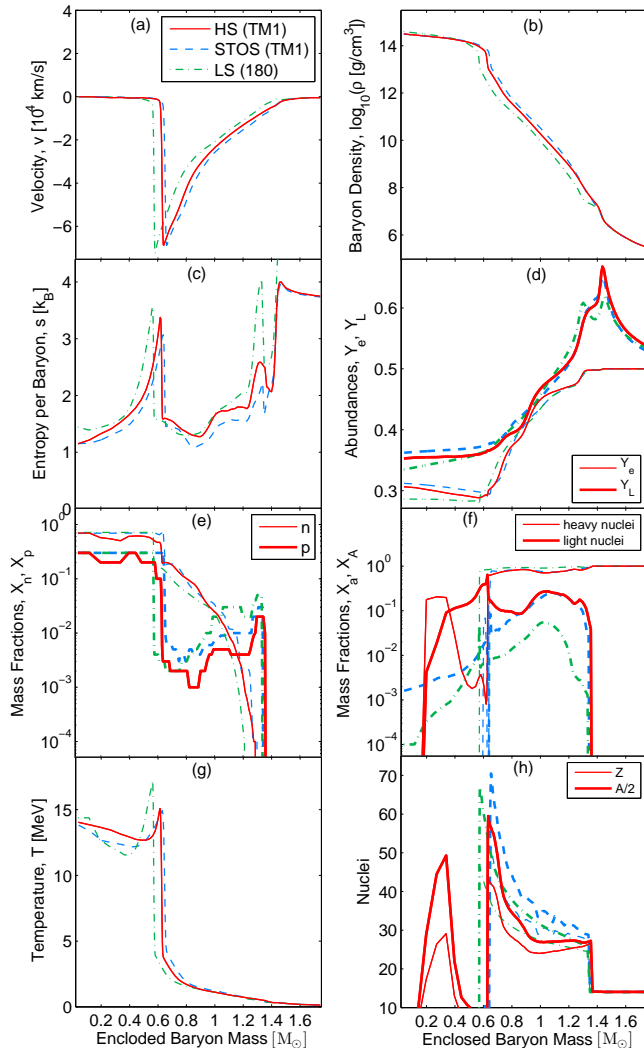


FIG. 6.— Same as Fig. 4 but at bounce, defined as the moment when the maximum central density is obtained at the end of the iron-core collapse.

to the lower electron fraction at the center. As electrons provide a large contribution to the pressure at saturation density, the pressure in HS is lower, leading to more compression and larger temperatures. We emphasize again that STOS and HS are identical above saturation density. For the very soft non-relativistic LS, the same differences to STOS appear but are even more pronounced: the shock forms at smaller mass, the infall velocities are larger, and the central densities are higher. The central conditions at bounce, comparing the three EOS, are listed in Table 3, whereas s denotes the entropy per baryon. We conclude that even though HS and STOS are based on the same nucleon interactions, the different description of non-uniform nuclear matter and nuclei leads to a different evolution of the iron-core collapse. HS has a lower central electron fraction, which results in a more compact configuration at bounce.

Regarding the composition there are two main differences between HS, and STOS and LS: in the mass shells where the shock has ran through in HS there is a significant fraction of more than 10% of light nuclei present. The alpha-particle fraction of LS and STOS is almost

TABLE 3
SELECTED CENTRAL HYDRODYNAMIC QUANTITIES AT BOUNCE FOR THE 15 M_{\odot} MODELS

EOS	ρ [10^{14} g/cm 3]	s [k_B]	Y_e	M^a [M_{\odot}]
LS (180)	3.948	1.4463	0.2860	0.5799
STOS (TM1)	3.061	1.1512	0.3120	0.6586
HS (TM1)	3.135	1.1484	0.3063	0.6258

Note.

^aBaryon mass enclosed inside the shock.

two orders of magnitude smaller (see Fig. 6(f)). Obviously, such a large abundance of light nuclei influences the EOS. The second main difference in the composition of the different EOS concerns heavy nuclei. At densities larger than 10^{14} g/cm 3 there is a small region where heavy nuclei appear in HS (see Fig. 6(h) between 0.2 and 0.4 M_{\odot}). This can be seen as the beginning of the uniform nuclear matter phase and part of the transition to uniform nuclear matter. Instead in STOS and LS no heavy nuclei form behind the shock. One observes a different behavior of the transition to uniform nuclear matter in HS in comparison to LS and STOS. This is also the density regime, where the formation of the nuclear pasta phases is possible. In HS the pasta phases are not taken into account, a Maxwell construction is used, and furthermore the transition depends crucially on the implementation of the excluded-volume effects. However, at these high densities neutrinos are trapped. Hence, the heavy nuclei at high densities should have a negligible effect on the neutrino transport especially since the heavy nuclei lie outside the approximated Gamow–Teller window of Bruenn (1985).

3.3. Post-bounce Evolution

Figure 7 shows the evolution for the three different EOS at 200 ms post bounce. The bounce shock stalls for all models and turns into the standing accretion shock, which stands around 100 km at 200 ms post bounce (see Fig. 7(a)). It separates the inner high-density and high-temperature core from the outer material which is being accreted. Note the entropy differences ahead of the shock between LS and STOS/HS, which are due to the aforementioned different treatment of non-NSE. During the long-term post-bounce evolution of several hundreds of milliseconds, the standing accretion shocks contract in a similar fashion for all EOS under investigation and hence the profiles become increasingly similar. The differences obtained at bounce due to the different composition and different description of nuclei remain in the post-bounce evolution. Matter is slightly more neutron-rich for HS than for STOS, and HS leads to higher central densities and temperatures. In comparison to LS, both HS and STOS are significantly stiffer. With LS the shock contracts much faster and the central density and temperature are much higher, as well as Y_e is lower (see Fig. 7(a), (b), (c) and (g)).

Also the composition still shows some similarities to the situation at bounce. The infalling matter is composed of heavy nuclei, which are systematically smaller for HS than in STOS and LS. The accreted matter is heated up and dissociates partly into alpha particles. When matter reaches the accretion front it encounters

strong shock heating, so that nuclei get dissolved and almost only free nucleons remain. Further inside the proto-neutron star the compression becomes strong enough that the fraction of light nuclei increases again. In general, alpha particles and light nuclei are favored in the innermost layers not only because of the higher densities, but also because of the lower entropies. In HS there is a small region slightly below saturation density where even heavy nuclei appear, before they dissolve into homogeneous nuclear matter at slightly higher densities. However, the fraction remains small, less than 20 % (see Fig. 7(f)). Heavy nuclei cannot be found below the shock with STOS or LS at the shown time. But also with STOS heavy nuclei are present inside the core with significant mass fractions but only from shortly after bounce until roughly 50 ms post bounce, when they disappear again. For STOS on the other hand, alpha particles extend down to the center of the proto-neutron star in Fig. 7(f). In this model, due to the different description of the excluded volume effects, alpha particles can also exist slightly above saturation density. However, more sophisticated studies show that the Mott transition actually occurs at lower densities (Typel et al. 2010).

By looking at the electron fraction in more detail, one sees that the envelope of the proto-neutron star below the standing bounce shock has a larger electron fraction with HS than in STOS. This can be attributed to the larger symmetry energy of HS in comparison to STOS, due to the inclusion of the additional light nuclei besides alpha particles in the HS model. Light nuclei exist as additional degrees of freedom for symmetric nuclear matter, which lower the chemical potential of symmetric nuclear matter and therefore decrease the Q -values of electron captures. As charged-current reactions on light nuclei are not taken into account in the present investigation, this leads to less electron captures than in STOS. We see in Fig. 7(f) that the fraction of light nuclei in HS behind the shock is roughly two orders of magnitude larger than in STOS (and LS). At $R \sim 20$ km the light nuclei fraction increases beyond 10 % in the NSE models, but jumps to zero between 10 and 20 km, because in the HS EOS nuclei are neglected for $T > 20$ MeV for simplicity.

3.4. Nuclear Composition from Collapse to Post Bounce

Figure 8 gives a more detailed view of the contribution of light nuclei to the EOS. The mass fractions of the most important light nuclei with $Z \leq 3$ are plotted for the simulation with HS (TM1). The black lines depict the particles which are also included in LS and STOS, and the blue lines depict light nuclei, which were usually not considered in core-collapse supernova simulations until now. We want to emphasize that all mass fractions which are shown in this article are a direct output from the EOS applied in the simulations. In Fig. 8, one sees that additional light nuclei apart from alpha particles are negligible at the progenitor stage. This explains also the good agreement for the fraction of light nuclei in Figs. 2 and 3. However, at later times during the core collapse where temperature and density increase sufficiently, other light nuclei in addition to alpha particles appear in non-negligible fractions on the order of a few percent and they can become even more abundant than alpha particles. In general, the favored appearance

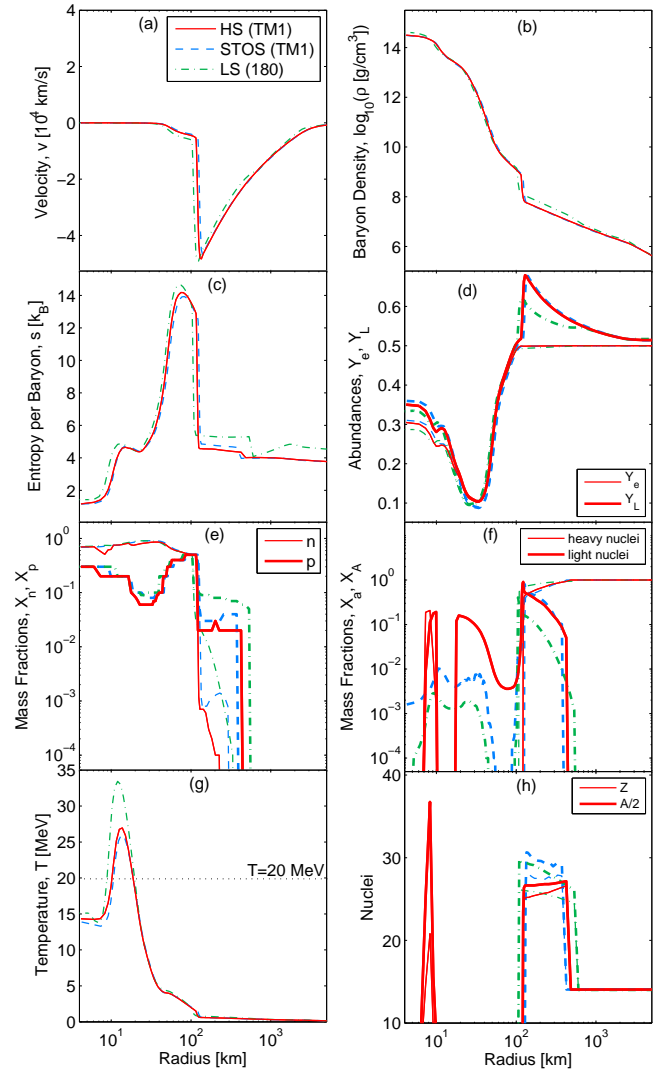


FIG. 7.— Radial profiles of selected hydrodynamic quantities with respect to the radius for the $15 M_{\odot}$ progenitor model from Woosley and Weaver (1995) at 200 ms post bounce. The same notation as in Fig. 2 is used.

of weakly bound light nuclei instead of alpha particles is driven by the increased entropy of a system composed of smaller fragments, where binding energies play only a minor role. How does this work?

Using Maxwell-Boltzmann distribution functions for nuclei, schematically the number density of a nucleus of mass A is

$$n_A \propto A^{3/2} \exp\left(A \frac{B_A + \mu}{T}\right), \quad (14)$$

where μ is the nucleon chemical potential without rest mass and $B_A > 0$ the binding energy per nucleon of nucleus A . We remark that $B_A + \mu$ is always negative in our calculations. Thus we do not see any indication for Bose-Einstein condensation and the use of Maxwell-Boltzmann statistics is justified. For any given finite temperature, in the limiting case of vanishing density, μ will be so negative that $e^{A\mu/T}$ is completely dominating and the binding energies are negligible. Only free neutrons and protons will be present. This is an entropy effect,

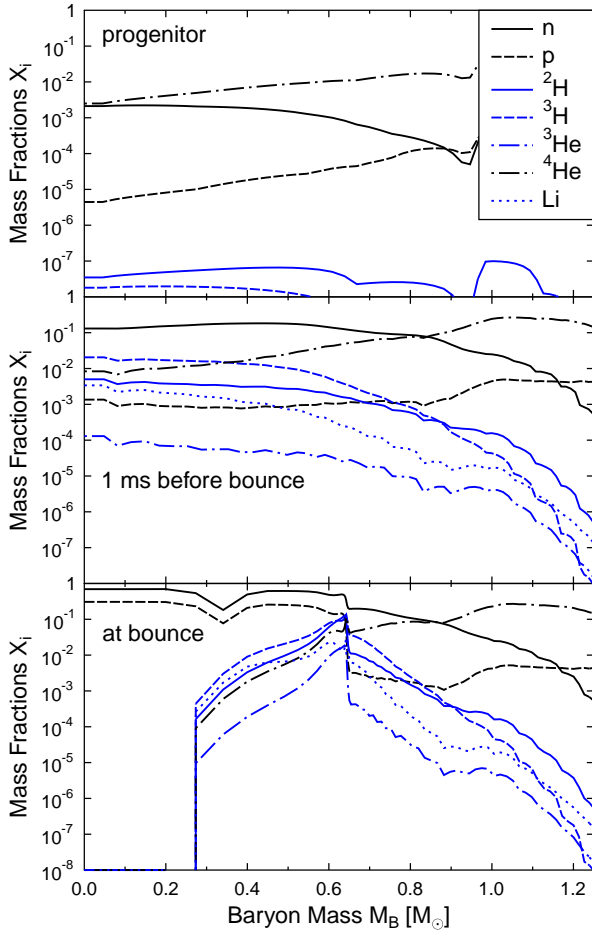
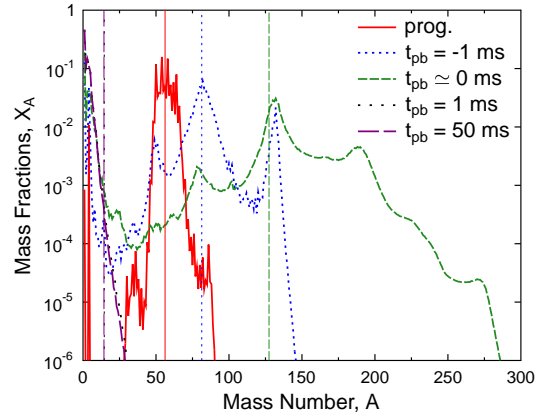


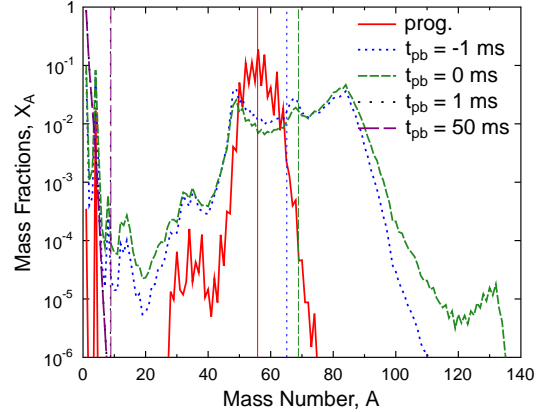
FIG. 8.— Radial profiles of the mass fractions of the most important light nuclei with $Z \leq 3$ in the HS (TM1) EOS for the core-collapse simulation of the $15 M_{\odot}$ from Woosley and Weaver (1995), at the progenitor stage (top), during the collapse (middle) and at bounce (bottom). “Li” shows the sum of the mass fractions of all lithium isotopes.

as a result of the minimization of the free energy. With increasing density the role of temperature decreases and at some point it is favorable to form nuclei, because the internal energy contribution to the free energy becomes dominating over the entropy contribution. Let us imagine that all nuclei had the same binding energy per nucleon B . In this scenario, the average mass number of the distribution of nuclei would increase continuously with density. Thus naturally there would be a certain density, where deuterons gave the main contribution to the composition, followed by alpha particles at larger densities. For sufficiently large temperatures $T \gtrsim B_A$, so that the differences in binding energies per nucleon of light nuclei can be seen as small corrections, this scenario gives a viable explanation for the large mass fractions of weakly bound light nuclei observed in our simulations. Contrary, for low temperatures $T < B_A$, the strong binding energy of the alpha particle is so dominant that other light nuclei will never give the main contribution to the composition.

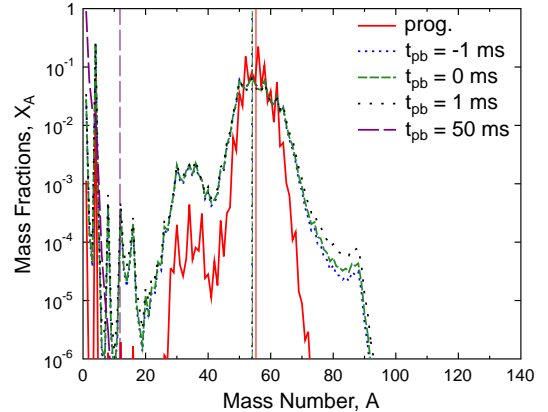
It is also instructive to realize that for any given finite temperature there is always a certain density where the mass fractions of deuterons and alphas are equal. This happens approximately at a chemical potential of $\mu \sim B_d - 2B_{\alpha} \sim -14$ MeV, where the difference of the



(a) $M_B = 0.6 M_{\odot}$



(b) $M_B = 0.8 M_{\odot}$



(c) $M_B = 1.0 M_{\odot}$

FIG. 9.— Mass fraction distribution of the HS (TM1) EOS for three different mass shells, and five different times, ranging from the progenitor to 50 ms post bounce. The vertical lines show the corresponding average mass number of heavy nuclei.

total binding energies is compensated by the difference in total chemical potentials. At higher densities, the alpha fraction is larger, at lower densities the deuteron fraction. With increasing temperature this point moves to higher densities. Thus only for sufficiently large temperatures the fractions of deuterons and alphas will be comparable to the mass fraction of unbound nucleons. In conclusion, the significant appearance of weakly bound light nuclei is driven by an interplay of temperature and density effects.

Let us come back to the discussion of Fig. 8. At 1 ms

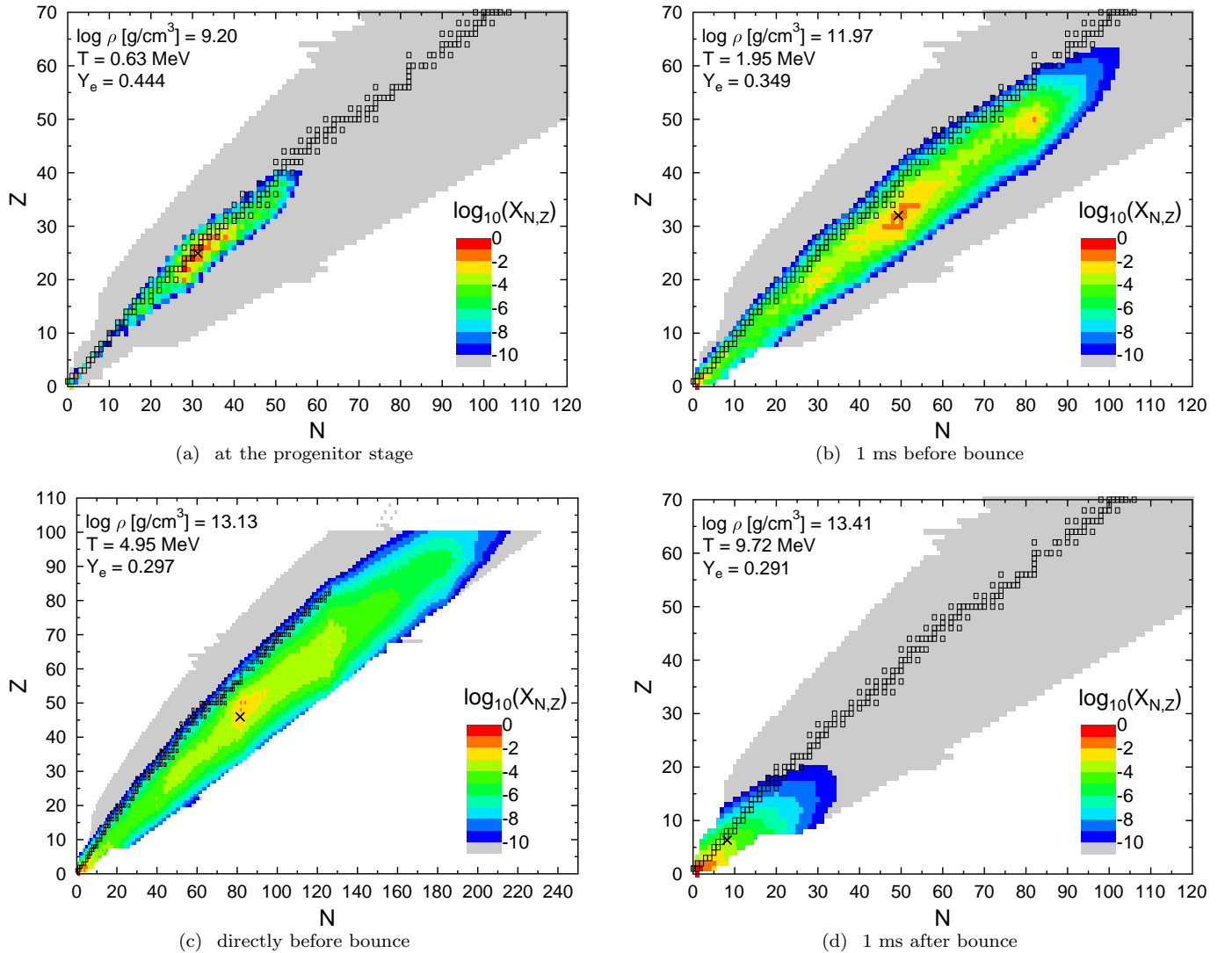


FIG. 10.— Distribution of the mass fractions of nuclei in the HS (TM1) EOS for the mass shell of $M_B = 0.6 M_\odot$ and four selected times, which are also shown in Fig. 9(a). Gray filled squares correspond to nuclei which are included in the HS (TM1) EOS, but which have a mass fraction below 10^{-10} . The crosses mark the average of the distribution of heavy nuclei and the black squares show stable nuclei as a reference.

before bounce, temperatures above 5 MeV are reached at the center (see Fig. 5) which are sufficiently high so that light nuclei can form at large densities. From Fig. 8 one sees that tritium (^3H), alphas (^4He), deuterium (^2H), and lithium (Li) appear in similar concentrations in the innermost layers of the collapsing core. The largest fractions are reached for ^3H because matter becomes increasingly neutron rich during the core-collapse phase. We want to emphasize that the alpha particle is less abundant than deuterium, tritium and the summed lithium isotopes in the center. Only in the outer layers the composition is dominated by alpha particles.

At bounce (bottom of Fig. 8) we see that the formation of the shock enhances the appearance of unbound nucleons due to the increased central densities and temperatures. At this stage, the matter behind the shock, which is located at $\sim 0.6 M_\odot$, is heated to roughly 14 MeV (see Fig. 6). Almost all heavy nuclei get dissociated, but the fractions of light nuclei are increased. Note that the den-

sities are very large $\sim 10^{14} \text{ g/cm}^3$. At low densities there would be no light nuclei for such large temperatures any more, but here we have a competition between density and temperature effects, as described before. At the very center of the collapsing stellar core, at densities above saturation density, light nuclei disappear completely and uniform nucleon matter is reached.

Regarding the contribution of heavy nuclei, with the HS EOS we can study the impact of the commonly used SNA. Figure 9 shows the mass distributions of nuclei with the HS (TM1) EOS for the (baryonic) mass shells of $0.6, 0.8,$ and $1.0 M_\odot$ at different times. Fig. 10 depicts the distributions in form of nuclear charts only for the $0.6 M_\odot$ mass shell. We want to concentrate on this mass shell first. At the progenitor stage (Fig. 10(a) and red solid lines in Fig. 9(a)) we clearly see that iron-group nuclei are most abundant, already mentioned in the discussion of Fig. 2. The distribution is still close to the valley of stability. During the ongoing contraction in

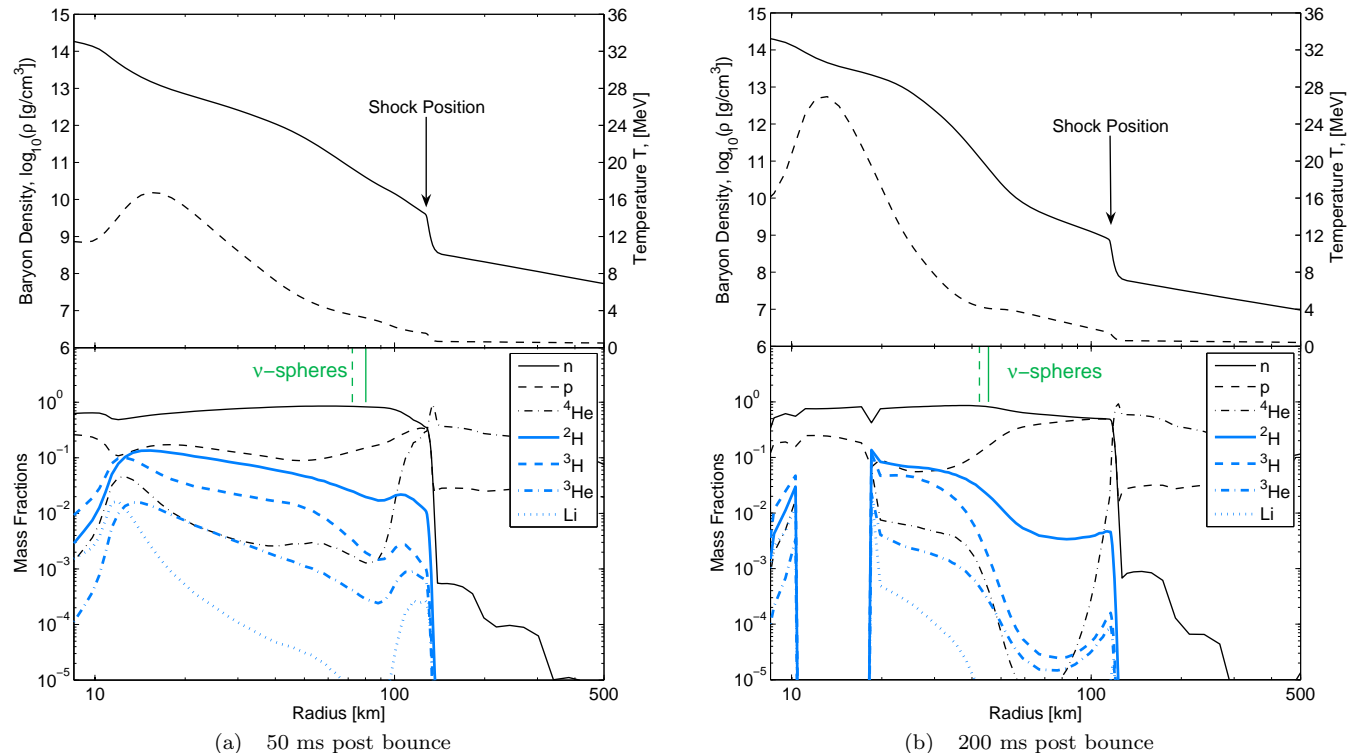


FIG. 11.— Radial profiles of the baryon density (solid lines) and the temperature (dashed lines) in the top panels and the corresponding nuclear composition regarding light nuclei (bottom panels) at two selected post-bounce times for the $15 M_{\odot}$ progenitor model from Woosley and Weaver (1995) using the HS (TM1) EOS. The green vertical lines denote the position of the neutrinospheres for ν_e (solid lines) and for $\bar{\nu}_e$ (dashed lines).

the core collapse, electron captures take place and the formation of heavier and more neutron-rich nuclei is favored. In Fig. 10(b), we see the importance of closed neutron shells, i.e. nuclei with $N = 50$ and $N = 82$ are most abundant. These nuclei correspond to the two peaks of the blue dotted lines in Fig. 9(a). Shortly before bounce, the distribution of heavy nuclei becomes very broad and goes beyond $A = 300$, which is nicely illustrated in Fig. 10(c). Note the different scale in this subfigure. Very exotic nuclei are found and the distribution is far away from the valley of stability. The most abundant nuclei are at the well-known neutron-magic number $N = 82$, but also other neutron-magic numbers (50 and 126) are strongly populated, visible by the additional peaks and bumps in the distribution shown by the green dashed lines in Fig. 9(a). Obviously, such multiple peaks and/or bimodal distributions cannot be captured by an average heavy nucleus, depicted by vertical lines in Fig. 9 and crosses in Fig. 10.

Another interesting aspect of heavy nuclei is the largest mass numbers which are reached in the simulations. Furusawa et al. (2011) pointed out that they obtain nuclei with mass number up to 2000 in their EOS and even larger nuclei are present in the STOS EOS. Superheavy nuclei with A up to 3000 are also found in the Hartree calculations by G. Shen et al. (2011b). Contrary, in HS it is impossible to obtain such superheavy nuclei, due to the use of nuclear mass tables based on experimental data and nuclear structure calculations. At the times shown in all the previous plots the maximum average mass numbers are around 250, whereas all EOS lie in

a similar range. However, in Fig. 10(c) one sees that the distribution of heavy nuclei in HS reaches the border of the mass table. The overall maximum mass numbers which we get during the entire simulation are $A \sim 900$ for STOS, but only $A \sim 300$ for HS (TM1) and $A \sim 200$ for LS. For all three EOS these overall maximum mass numbers are found at similar conditions, at ~ 0.5 ms before bounce and $M_B \sim 0.1 M_{\odot}$. From this point until bounce the mass numbers decrease, see Fig. 6. In the early post-bounce evolution of STOS there is a period where heavy nuclei appear again in the core at densities around 10^{14} g/cm³, i.e., in the transition region to uniform nuclear matter. At 50 ms post bounce these heavy nuclei have disappeared again, therefore they cannot be seen in the previous figures. This appearance of heavy nuclei is similar like the peak in the mass fraction of heavy nuclei with HS below the shock in Figs. 6 and 7, but for HS it persists for a much longer time. Furthermore, in STOS these nuclei are superheavies with mass numbers up to 500. In general we find that neutrinos are trapped under the conditions where superheavies appear, and thus they do not have an effect on the neutrino transport. Therefore we do not expect that the limitation of HS to nuclei with mass numbers up to ~ 300 is crucial for the supernova dynamics.

We turn back to the evolution of the nuclear distribution of the mass shell shown in Fig. 10. At bounce, the shock forms very close to $0.6 M_{\odot}$. Almost immediately after the stage depicted in Fig. 10(c), the shock runs through the selected mass shell and most of the heavy nuclei get dissociated (Fig. 10(d)). A distribution

of light nuclei forms, with mass fractions which decrease exponentially with increasing A (Fig. 9(a)). This form of the distributions at 1 and 50 ms post bounce indicates that the binding energies are not very important any more, due to the high temperatures. When the shock propagates outward and dissociates the infalling matter, the distributions change from the very broad shape with peaks due to binding energy and shell effects to a simple exponential. The change of the shape of the distributions can also not be captured by the average of the heavy nuclei. For the higher mass shells shown in Figs. 9(b) and 9(c), similar features are observed but at later times. Furthermore, the mass numbers reached are significantly smaller for the outer mass shells, because matter is much less compressed. Animated results of the nuclear distributions of different mass shells can be found at the aforementioned HS EOS Web site.

Also in the post-bounce evolution light nuclei give an important contribution to the composition, as can be seen from Figs. 11(a) and 11(b). Again, the standard particles which are usually considered in a core-collapse supernova are shown in black, and the additional new light nuclei in blue. One can identify three different regions: the core of the newly born proto-neutron star at the center up to $R \sim 10$ km, the envelope of the proto-neutron star up to the standing accretion shock at $R \sim 200$ km, and the infalling matter in the outer layers. The core is composed of mainly free nucleons and some light nuclei which disappear at densities larger than saturation density. The accreted matter is a mixture of mainly heavy nuclei, alpha particles and free protons at low abundances. However, behind the standing accretion shock the sudden increase of temperature dissociates heavy nuclei into smaller fragments, a mixture of nucleons and light nuclei appears. Note that ${}^3\text{H}$ is the most abundant light nucleus in the proto-neutron star, whereas ${}^2\text{H}$ dominates the shock heated low-density matter which is more symmetric. The ${}^2\text{H}$ fraction is usually at least one order of magnitude larger than the alpha-particle fraction.

3.5. Impact on Neutrino Heating and Cooling

The presence of light nuclei can modify neutrino heating and cooling. In the present article, we do not include any inelastic weak processes on light nuclei, but the detailed knowledge of their abundances gives already first insight into the possible impact they might have on neutrino heating and cooling. The heating region is located between the neutrinospheres and the standing bounce shock, whereas cooling occurs around the neutrinospheres. To identify the abundances of light nuclei in the two regions, in Figs. 11(a) and 11(b) we also show the neutrinospheres (see the vertical lines, ν_e : solid lines, $\bar{\nu}_e$: dashed lines). During the earlier post-bounce phase (see bottom panel of Fig. 8), ${}^2\text{H}$ and ${}^3\text{H}$ are as abundant as protons right behind the still expanding bounce shock. There, the inclusion of inelastic weak processes with light nuclei, i.e., inelastic scattering and most dominantly charged-current reactions, may modify the neutrino heating. However, already at 50 ms (Fig. 11(a)) the abundances directly below the shock have decreased and the neutrino flux is already quite diluted geometrically at this distance close to the shock. The most efficient heating occurs at smaller radii, where there are much

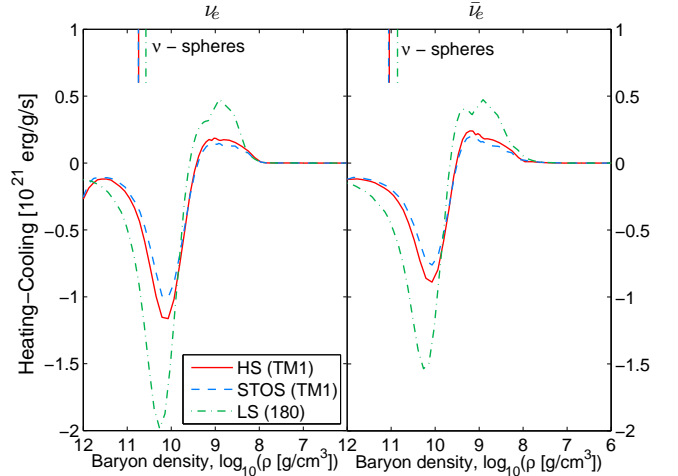


FIG. 12.— Heating-cooling rates, i.e., the net energy deposition by neutrinos for the $15 M_{\odot}$ progenitor models at 200 ms post bounce, comparing the different EOS under investigation. The vertical lines show the neutrinospheres.

less light nuclei than free protons.

The abundance of light nuclei in the heating region decreases further on the long term. The slight compression of the surface of the PNS which is seen in Figs. 11(a) and 11(b) decreases the density close to the shock, leading to a dissolution of light nuclei into nucleons. At 200 ms post bounce, above the neutrinospheres only few light nuclei are found in comparison to the free nucleons. Hence a very strong impact on neutrino heating is not expected during the later post-bounce phases. Nevertheless it is interesting to note that in Fig. 11(b) the largest difference between the alpha-particle fraction and the fractions of additional light nuclei is observed in the heating region between the neutrinospheres and the standing bounce shock. There, the fraction of alpha-particles is up to three orders of magnitude smaller than the fraction of deuterium. The largest contributions of light nuclei in the post-bounce evolution are found below the neutrinospheres. There, e.g., deuterium is still as abundant as protons. It may modify cooling and could have an effect on the explosion dynamics. For example, less cooling has a similar potential than more heating. Additionally, an impact on cooling is interesting because it modulates the neutrino signal. Furthermore, it may be of particular interest for studies that investigate the long-term evolution of proto-neutron stars, during which the neutrinospheres move continuously to higher densities where light nuclei are more abundant. The conclusions about the possible impact of light nuclei on the supernova dynamics are only qualitatively and should be investigated in more detail (including inelastic weak processes with light nuclei) in future studies.

Apart from the composition also the EOS affects the heating and cooling via the compactness of the proto-neutron star. This is shown in Fig. 12 where we plot the heating-cooling rates for ν_e (left panel) and $\bar{\nu}_e$ (right panel) with respect to the baryon density, at 200 ms post bounce. It becomes clear that the largest heating below the standing bounce shock (which is located around $\rho \simeq 10^8$ g/cm 3) but also the largest cooling rates at the neutrinospheres are obtained for the soft LS (180) EOS.

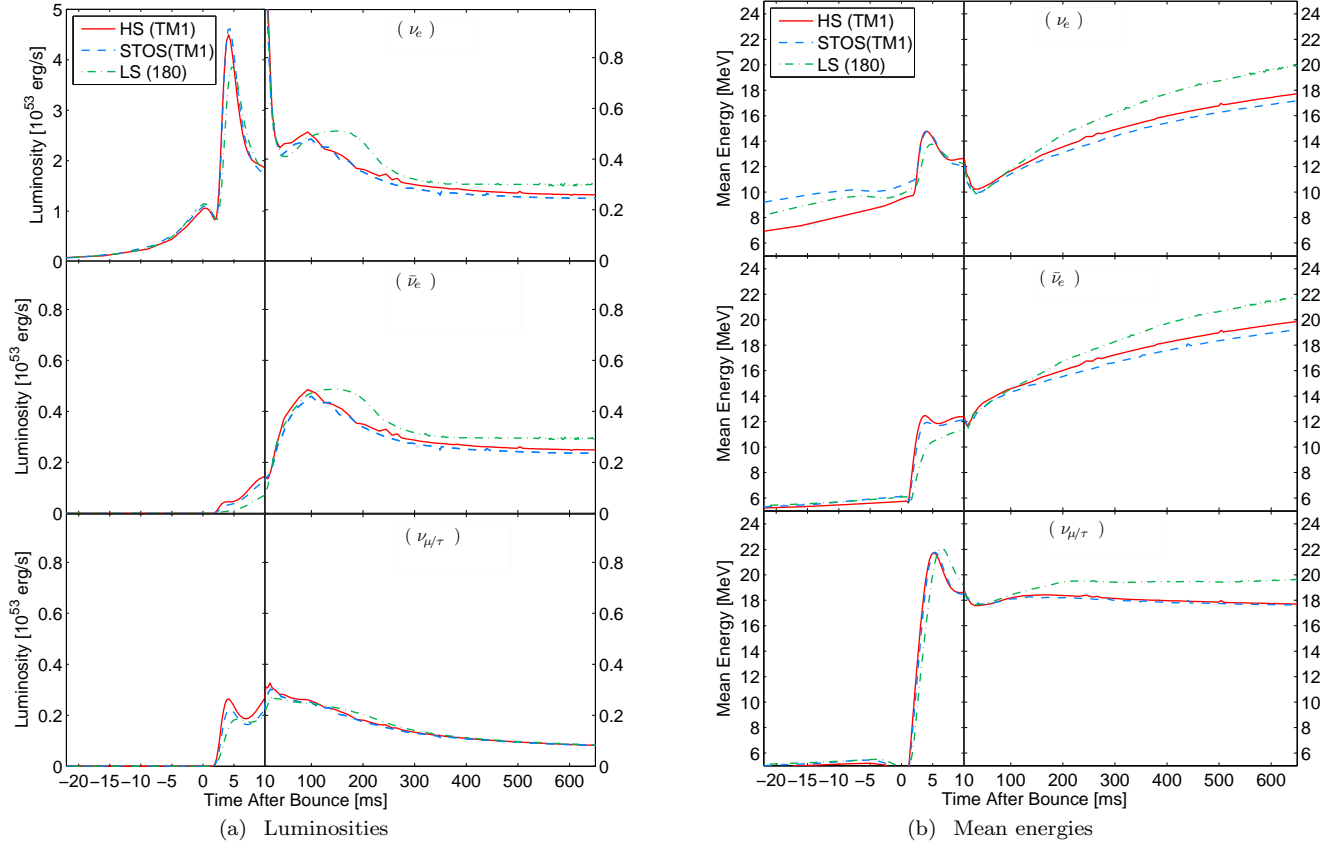


FIG. 13.— Evolution of the neutrino luminosities and root-mean-square energies for the $15 M_{\odot}$ progenitor model from Woosley and Weaver (1995), comparing the HS (TM1) EOS (red solid lines), the STOS (TM1) EOS (blue dashed lines), and the LS EOS (dash-dotted green lines). The observables are sampled in a co-moving reference frame at a distance of 500 km. Note the two different scales in the subfigure for the electron neutrino luminosities.

Although STOS (TM1) and HS (TM1) are both based on the same RMF parameterization TM1, the slightly more compact proto-neutron star of HS leads to larger heating and cooling rates for HS.

3.6. Neutrino Signal

Figures 11(a) and 11(b) show that neutrons and protons are the most abundant particles at the neutrinospheres, but also ^2H and ^3H appear at non-negligible abundances of 10^{-1} to 10^{-2} . Consequently, the inclusion of the weak processes with light nuclei which are not incorporated in the present study may modify the neutrino signal. Here, we will identify the impact of the three EOS on the neutrino signal. Several aspects related to the comparison of the neutrino signal of STOS and LS have already been discussed in Sumiyoshi et al. (2008) and Fischer et al. (2009) for various massive iron-core progenitor models from different groups. Here we will add the differences and similarities between HS and STOS as well as LS to the discussion.

Figure 13 depicts the neutrino signal, i.e., the evolution of luminosities and mean energies, for the $15 M_{\odot}$ progenitor comparing the three reference EOS under investigation. Note the two different scales in the subfigure for the electron neutrino luminosity (top panel of Fig. 13(a)). Let us first look at the collapse phase before bounce during which only ν_e are produced via electron captures at heavy nuclei and free protons. The earliest

time which is shown in Fig. 13 corresponds to a stage between Fig. 4 ($t_{\text{pb}} \sim -40$ ms) and Fig. 5 ($t_{\text{pb}} \sim -1$ ms). If we look at the top panel of Fig. 13(b) we see that the mean energies of electron neutrinos are about 1.5 MeV smaller comparing HS with LS and about 2 MeV smaller comparing HS with STOS. This is related to the conditions at decoupling at the neutrinospheres R_{ν} during the core-collapse phase, where we find the following ordering: $\rho_{R_{\nu_e}}^{\text{HS}} > \rho_{R_{\nu_e}}^{\text{STOS}} \geq \rho_{R_{\nu_e}}^{\text{LS}}$, $T_{R_{\nu_e}}^{\text{HS}} \geq T_{R_{\nu_e}}^{\text{LS}} > T_{R_{\nu_e}}^{\text{STOS}}$, and $R_{\nu_e}^{\text{HS}} < R_{\nu_e}^{\text{STOS}} \simeq R_{\nu_e}^{\text{LS}}$. Since low-energy neutrinos decouple generally at high densities and temperatures with small neutrinosphere radii, the following hierarchy holds for the mean energies $\langle E \rangle_{\nu_e}^{\text{HS}} < \langle E \rangle_{\nu_e}^{\text{LS}} < \langle E \rangle_{\nu_e}^{\text{STOS}}$. The electron neutrino luminosities which are also shown in Fig. 13(a) are determined by mass accretion. During the collapse phase the differences in the mass accretion rates are small for the different EOS and the ordering of the neutrinospheres leads to the following hierarchy for the luminosities $L_{\nu_e}^{\text{HS}} < L_{\nu_e}^{\text{STOS}} \leq L_{\nu_e}^{\text{LS}}$. During the first 10 ms after bounce, when the shock runs through the neutrinospheres, the ν_e -deleptonization burst is released. We find that the luminosities and mean energies of LS are lowest with maximum $L_{\nu_e} \simeq 4 \times 10^{53}$ erg/s, whereas HS and STOS are very similar with maximum $L_{\nu_e} \simeq 4.5 \times 10^{53}$ erg/s.

During the later post-bounce evolution, ν_e and $\bar{\nu}_e$ are produced mainly via electron captures at protons

and positron captures at neutrons. Their luminosities are given by mass accretion at the corresponding neutrinospheres. The following hierarchy holds for the mass accretion rates at the neutrinospheres $\dot{m}_{R_{\nu_e/\bar{\nu}_e}}^{\text{LS}} > \dot{m}_{R_{\nu_e/\bar{\nu}_e}}^{\text{HS}} \geq \dot{m}_{R_{\nu_e/\bar{\nu}_e}}^{\text{STOS}}$. Note also the ordering of the neutrinosphere radii, $R_{\nu}^{\text{LS}} < R_{\nu}^{\text{HS}} < R_{\nu}^{\text{STOS}}$. The different mass accretion rates are related to the different post-bounce conditions obtained for the different EOS. LS leads to the most compact configuration where the standing bounce shock contracts fastest which in turn leads to the highest mass accretion rate. The opposite holds for STOS, and HS lies between LS and STOS. Note that the small differences between HS and STOS are due to the different description of light and heavy nuclei at low and intermediate densities, which leads to slightly lower Y_e and a slightly more compact configuration for HS. Hence, $L_{\nu_e/\bar{\nu}_e}^{\text{LS}} > L_{\nu_e/\bar{\nu}_e}^{\text{HS}} \geq L_{\nu_e/\bar{\nu}_e}^{\text{STOS}}$ throughout the entire post-bounce phase shown in Fig. 13(a) up to 650 ms. On the other hand, $\nu_{\mu/\tau}$ are produced by pair processes and they interact only via neutral-current reactions. They decouple at generally higher densities. Consequently their neutrinospheres are deeper inside the proto-neutron star than the electron flavor neutrinospheres. The $\nu_{\mu/\tau}$ luminosity can be expressed in terms of diffusion which scales as $R_{\nu_{\mu/\tau}}^2 T^4|_{R_{\nu_{\mu/\tau}}}$. Here, higher temperatures at the neutrinospheres are compensated by smaller neutrinosphere radii and hence the luminosities have similar values for all EOS under investigation during the post-bounce evolution shown in Fig. 13(a) up to 650 ms.

The ordering of the mean energies of the different EOS is the same as for the luminosities. It reflects the ordering of the temperatures at the neutrinospheres. However, mean energies of (μ/τ) -neutrinos for LS are significantly higher than for HS and STOS. Note that (μ/τ) -neutrinos are sensitive to differences at high densities, where the EOS under investigation lead to different proto-neutron star contraction behaviors. The significantly faster proto-neutron star contraction for LS, in comparison to HS and STOS, leads to the higher (μ/τ) -neutrinos mean energies shown in Fig. 13(b). The contraction behavior for HS and STOS is more similar at high densities, leading to almost equal mean (μ/τ) -neutrino energies.

4. RESULTS: DIFFERENT NUCLEAR INTERACTIONS

The EOS imprint on the neutrino signal for the 15 M_{\odot} progenitor is rather weak. However, if we go to the regime of failed supernovae of very massive progenitors, the influence of the EOS becomes more pronounced, as was also found in previous EOS studies, like, e.g., by Sumiyoshi et al. (2007), Fischer et al. (2009), and O’Connor & Ott (2011). In order to illustrate and understand the effect of the high-density EOS on the emitted neutrino signal from core-collapse supernovae, we simulate the collapse of the massive 40 M_{\odot} progenitor from Woosley and Weaver (1995) which eventually ends up in a black hole. For such a massive progenitor, very high densities and temperatures are reached, where different EOS show significant differences. We want to emphasize that this is the first time that the non-relativistic LS EOS are compared with several different RMF EOS, giv-

TABLE 4
SELECTED CENTRAL HYDRODYNAMIC QUANTITIES AT BOUNCE FOR THE 40 M_{\odot} MODELS

EOS	ρ [10^{14} g/cm 3]	s [k_B]	Y_e
LS (180)	3.855	1.487	0.2844
LS (220)	3.674	1.475	0.2826
HS (FSUgold)	3.151	1.529	0.2815
HS (TMA)	2.878	1.545	0.2811
STOS (TM1)	2.690	1.505	0.2915

ing a more comprehensive view of EOS effects. On the other hand, we do not explore the important sensitivity on the progenitor star which was thoroughly studied by O’Connor & Ott (2011).

From the relativistic EOS models we apply STOS (TM1) and the two new EOS tables HS (TMA) and HS (FSUgold). Because HS (TM1) and STOS (TM1) are identical at high densities, we do not include HS (TM1) in the comparison any more. The two new EOS tables HS (TMA) and HS (FSUgold) have been introduced in §2.3 and §2.4, and selected EOS properties are listed in Table 2. We consider two different versions of the non-relativistic LS EOS in the comparison, LS (180) and LS (220), characterized by different values of the incompressibility (see Table 2). However, the simulation with LS (220) is performed with a lower resolution where we use only four neutrino propagation angles, because for this model we restrict the discussion on hydrodynamical aspects.

The most important hydrodynamical quantities at the core bounce of the five different EOS are given in Table 4. If one compares these values with the EOS properties of Table 2, one sees that LS (180) with the lowest incompressibility has the highest central density at bounce, followed by LS (220) and then FSUgold which has an incompressibility of 230 MeV. For TM1 and TMA the correlation between the density at bounce and the incompressibility is inverted. TM1 has the lowest density, even though the incompressibility of TMA is the largest. This has two reasons: here, we have asymmetric nuclear matter and the large symmetry energy of TM1 stiffens the EOS. Furthermore, higher order terms for the expansion around saturation density for symmetric matter (e.g., the skewness) are larger in TM1, so that TM1 behaves stiffer, as also noted before in § 2.4. This example illustrates that it is generally not possible to explain the global properties of an EOS with single saturation parameters, especially when going to high densities and/or asymmetry.

The most interesting differences occur in the late post-bounce phase, shortly before collapse to a black hole. Here, one could expect that the maximum mass of a cold neutron star is correlated with the time until black hole formation and the corresponding neutrino signal, as was also found in previous studies of Sumiyoshi et al. (2007), Fischer et al. (2009), and O’Connor & Ott (2011). If this expectation was true, we should find the following sequence for the time until black hole formation: HS (FSUgold), LS (180), HS (TMA), LS (220), and STOS (TM1), in increasing order. Next we investigate the neutrino signal and try to identify such correlations.

The neutrino signals for the 40 M_{\odot} model using differ-

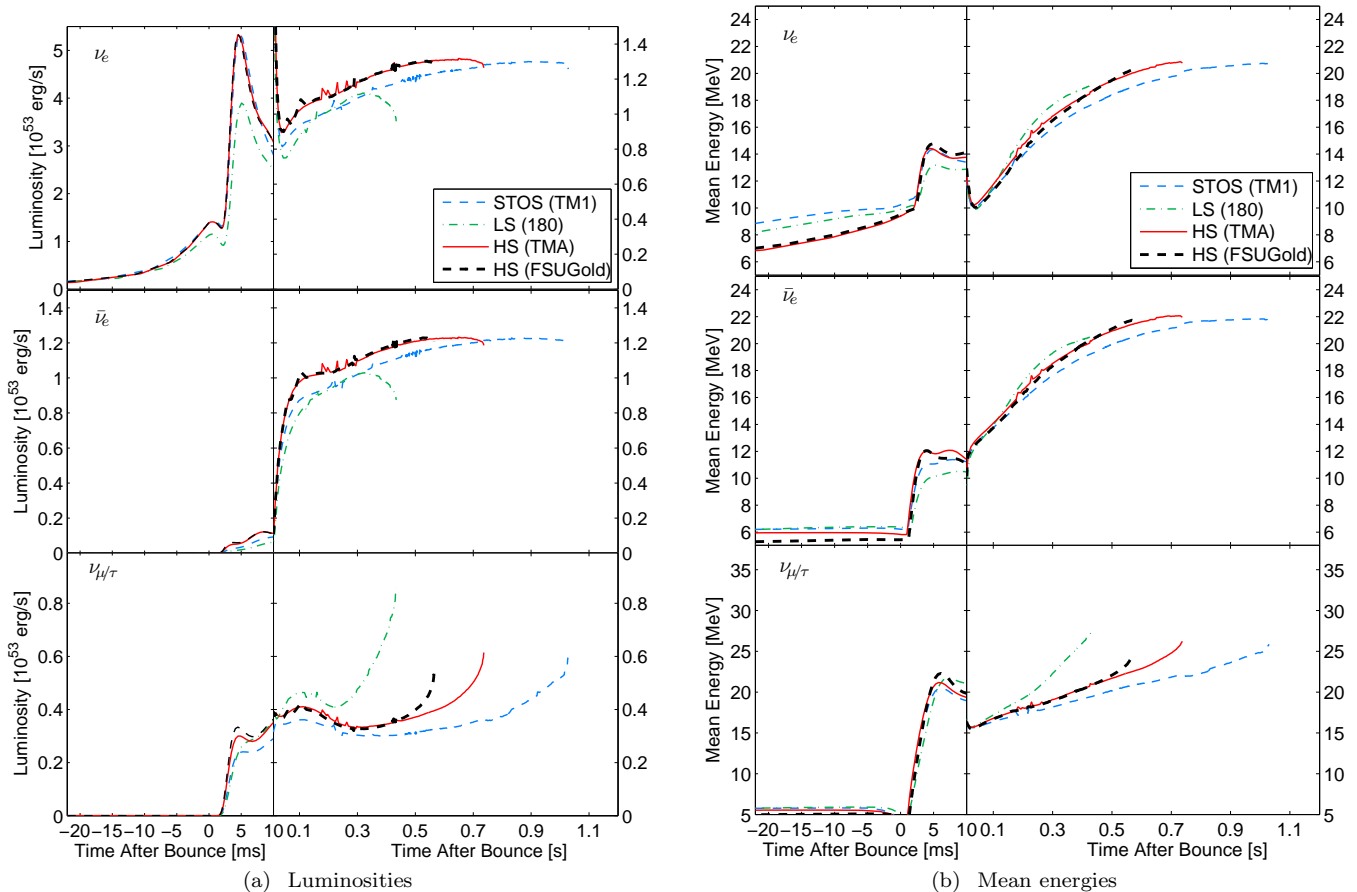


FIG. 14.— Evolution of the neutrino luminosities and mean energies for the $40 M_{\odot}$ progenitor model from Woosley and Weaver (1995), comparing the HS (TMA) EOS (red solid lines), HS (FSUGold) EOS (black dashed lines), the STOS (TM1) EOS (blue dashed lines), and the LS (180) EOS (dash-dotted green lines). The observables are sampled in a co-moving reference frame at a distance of 500 km. Note the two different scales in the subfigure for the electron neutrino luminosities.

ent EOS are shown in Fig. 14, similar to Fig. 13. LS (220) is not included in this figure, due to the reduced neutrino angular resolution in its simulation. We remark that the mean energies shown in Fig. 14(b) are always continuous. However, in the first milliseconds after bounce, they can change so quickly that this cannot be resolved in the scaling of the figure. The differences obtained during the core-collapse phase before bounce for the $40 M_{\odot}$ models are equivalent to what we have already discussed in the previous section at the example of the $15 M_{\odot}$ models. For the two HS models the neutrino light curves and evolution of the mean energies lie almost on top of each other, independent from the parameterization, until a certain level of compactness is reached. This also holds for the HS (TM1) EOS which is not shown here. It is very interesting that all HS EOS give a very similar neutrino signal even during the early post-bounce phase. The neutrino signal is generated at densities below saturation density, and even though the nascent proto-neutron star may be different for the different EOS, the imprint of the high-density phase is rather weak. Obviously, at low densities the interactions of unbound nucleons are not so important, whereas the description of nuclei and the degrees of freedom in the nuclear composition are crucial, which explains why the neutrino signal evolves so similar for the different HS models.

However, the moment of black hole formation is set by the nuclear interactions in the high-density region of the EOS. Figure 15 depicts the evolution of the central densities for the five different EOS. After bounce, the curves first show a linear behavior, until the newly born proto-neutron star becomes gravitationally unstable and collapses to a black hole. LS (180) shows a very fast compression in the center, followed by LS (220), then FSUGold, then TMA and finally TM1 with the slowest compression behavior. By approaching the moment of black hole formation a significant rise of the $\nu_{\mu/\tau}$ luminosities is observed. The different EOS have different timescales until black hole formation, and thus pronounced differences occur for the $\nu_{\mu/\tau}$ luminosities and mean energies, making μ/τ -neutrinos the best messengers of the EOS. Contrary, there is only little separation for the evolution of ν_e and $\bar{\nu}_e$ mean-energies for the four EOS, and also the luminosities remain more similar. Further details about the rise of the $\nu_{\mu/\tau}$ luminosities and its connection to the contraction of the proto-neutron star can be found in Liebendörfer et al. (2004) and Fischer et al. (2009).

Table 5 lists selected hydrodynamic quantities for the last stable configuration before the beginning of black hole formation. Here this is defined as the moment when infall velocities on the order of 1000 km/s are obtained in the PNS interior. We study the possible correlation

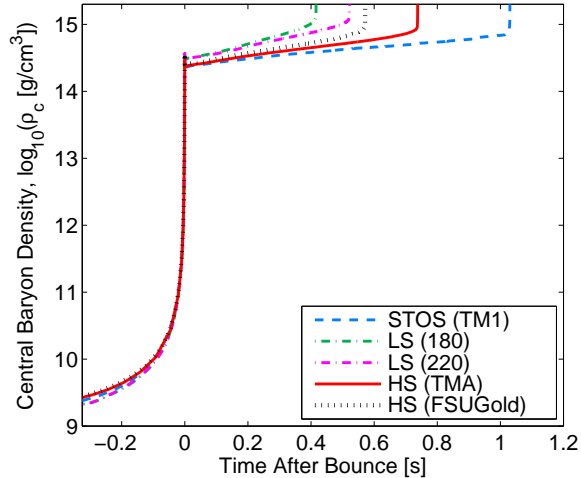


FIG. 15.— Evolution of the central density for the collapse of the $40 M_{\odot}$ progenitor model from Woosley and Weaver (1995), comparing the different EOS under investigation.

between the maximum mass of a cold neutron star and short/long accretion time until black hole formation by comparing t_{pb} and M_G from Table 5 with the maximum masses of cold neutron stars given in § 2.4. The results are shown in Fig. 17, where the black crosses depict the time until beginning of black hole formation as a function of the maximum gravitational masses of cold neutron stars. The maximum gravitational masses from Table 5 which were found in the simulations are shown by the blue squares. Compared to the cold configurations they are significantly increased for all EOS, but not equally strong. Surprisingly, although LS (180) has a larger maximum mass for a cold neutron star than FSUGold, and the maximum mass of LS (220) is larger than for FSUGold and TMA, the two LS EOS lead to the earliest beginning of black hole formation. In the supernova environment they behave less stable than the RMF EOS and even FSUGold gives a later black hole formation than both of them. FSUGold is followed by TMA and then comes TM1 with the latest collapse. Consequently, the expected ordering with the maximum mass of cold neutron stars established in the literature so far is not valid any more for our extended set of EOS including the new TMA and FSUGold EOS. The hierarchy between the maximum mass of cold neutron stars and short/long accretion times before black hole formation holds only separately within the class of RMF models or within the class of the non-relativistic LS EOS.

We want to examine this result further. In Table 5, the time until black hole formation and the enclosed baryon mass have the same ordering, which shows that the accretion rate is affected only little by the EOS. On the other hand the central densities at the onset of collapse are in most cases lower for the EOS which have a large mass at a later collapse. It illustrates the stiffness of the EOS for the conditions encountered here. Interestingly, for the central temperatures at the onset of collapse to a black hole, which are listed in Table 5, we find roughly 50 MeV for all three RMF EOS, but only 30 MeV for the two non-relativistic LS EOS.

The hydrodynamic state corresponding to the last stable configuration is further illustrated in Fig. 16. The

TABLE 5
SELECTED QUANTITIES AT THE ONSET OF COLLAPSE TO A BLACK HOLE

EOS	t_{pb}^{a} [s]	ρ^{b} [10^{15} g/cm 3]	T^{c} [MeV]	M_B^{d} [M_{\odot}]	M_G^{e} [M_{\odot}]
LS (180)	0.415	1.292	29.978	2.227	2.133
LS (220)	0.521	1.324	31.446	2.350	2.233
HS (FSUgold)	0.571	1.058	48.104	2.465	2.341
HS (TMA)	0.737	0.943	46.708	2.626	2.466
STOS (TM1)	1.028	0.769	49.705	2.864	2.652

Notes:

^aTime post bounce.

^bBaryon density in the center.

^cTemperature in the center.

^dBaryon mass enclosed inside the shock.

^eGravitational mass enclosed inside the shock.

similar behavior of the central temperatures of the RMF EOS and the different behavior of LS can be seen clearly. The peak temperatures around $M = 0.8 M_{\odot}$ are different for all five models. Interestingly, they show the same ordering like the central densities at core bounce in Table 4, namely, LS (180), LS (220), HS (FSUGold), HS (TMA), STOS (TM1) in decreasing order. This is also the sequence for the time until black hole formation. Note that the same ordering is also seen in the luminosities and mean-energies of μ/τ -neutrinos, which are most sensitive to temperature effects. The entropy profiles look more similar than the temperature profiles, whereas the two LS EOS lead to slightly higher entropies for $M_B > 0.5 M_{\odot}$. In Fig. 16 one can also identify the different central densities and different masses of the proto-neutron stars mentioned before. The electron fraction profiles show only small differences for the investigated EOS. The neutrino abundances are rather small and are also very similar for the different EOS.

We come to the unsatisfying conclusion that neither the incompressibility (comparing HS (TMA) and STOS (TM1)) nor the maximum masses of cold neutron stars can directly be related to the time until black hole formation. Single saturation properties are not sufficient to describe the behavior of the EOS in the simulation, where the different EOS evolve to different thermodynamic states. The maximum mass of cold neutron stars is not very meaningful, because the found states are very different from the cold configurations and because the strength of the temperature effects is model dependent as we will discuss in the next paragraph.

The profiles at the beginning of black hole formation from the simulations shown in Fig. 16 can roughly be approximated by a constant entropy per baryon of $s = 4 k_B$ and electrons in beta-equilibrium, where the contribution of neutrinos is negligible. We can compare the results from the simulations with hydrostatic configurations of the Tolman–Oppenheimer–Volkoff equations by using these approximations. The corresponding maximum masses are plotted in Fig. 17 versus the time until black hole formation, t_{BH} , from Table 5, by red circles. If one compares with the gravitational masses from the simulations which are depicted by blue squares, one sees that there is a rough agreement between “ $s = 4$ ” and “sim”. Furthermore, the time until black hole formation is monotonically increasing with $M_{\text{max}}(s = 4)$, similar

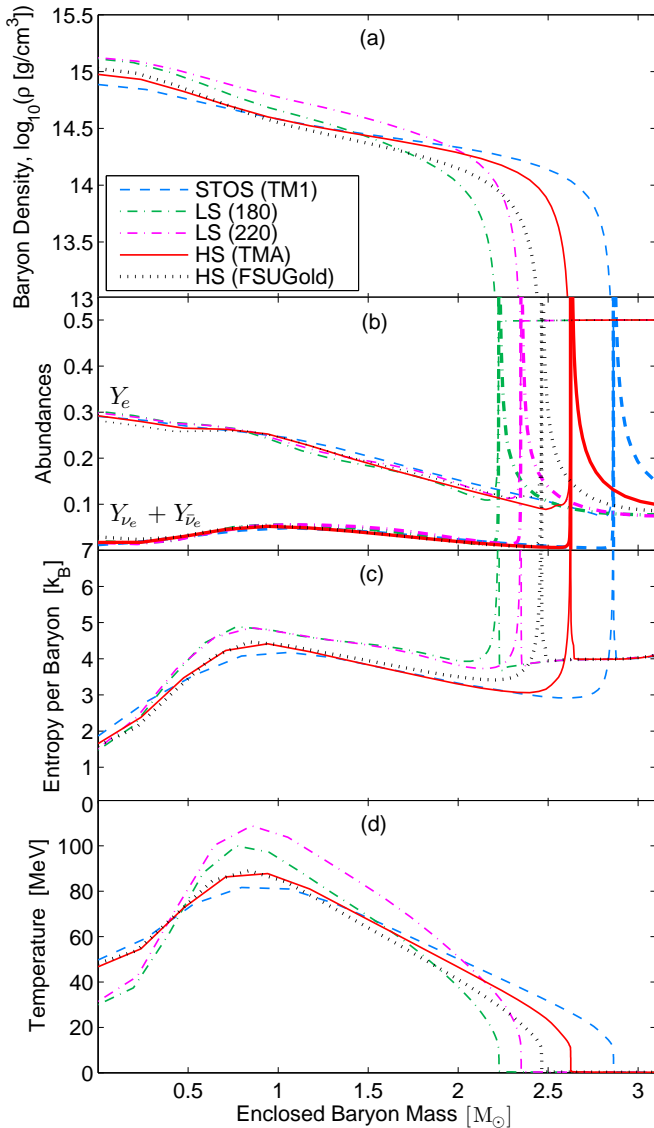


FIG. 16.— Selected quantities at the onset of collapse to a black hole of the $40 M_{\odot}$ progenitor model from Woosley and Weaver (1995), comparing the different EOS under investigation.

as for $M_{\max}(\text{sim})$. This shows that the above approximations ($s = 4 k_B$, beta-equilibrium without neutrinos) work sufficiently well to describe the states at the beginning of black hole formation from the simulations. In conclusion, the significant increase of the maximum mass in the simulation and the weak correlation between $M_{\max}(\text{cold})$ and t_{BH} is explained mainly as a temperature effect.

Very often for hydrostatic configurations of proto-neutron stars a constant entropy per baryon of $s = 2 k_B$ and electron lepton fraction $Y_L = 0.4$ is assumed. These conditions are clearly different to the profiles shown in Fig. 16 and are more appropriate for proto-neutron stars of less massive progenitors. We remark that such hydrostatic configurations with $s = 2 k_B$ and $Y_L = 0.4$ are indeed not suitable to explain the observed behavior. Their maximum masses are $0.3\text{--}0.5 M_{\odot}$ lower than observed in the simulations, and do not show a monotonic correlation with t_{BH} . A large entropy of $s = 4 k_B$ is the important point for the explanation, whereas the neutrino fraction

is less significant.

It is interesting that the non-relativistic LS EOS show less stiffening at finite entropy than the relativistic EOS. The different temperature profiles discussed before also indicate a different temperature dependency of the LS EOS. It is difficult to pin down whether this is an artifact of the non-relativistic dispersion relation or just a result of the chosen parameterization of the nuclear interactions. For example, the temperature–entropy relation depends on the effective nucleon mass m^* which appears in the dispersion relation. In LS the effective mass is set equal to the vacuum mass, $m^*/m = 1$, whereas m^*/m goes down to 0.2 in the core of the proto-neutron stars for the RMF models. The neglect of the effective mass reduction at finite density in LS leads to a suppression of temperature effects. In addition to the effective mass, also the electron fraction affects the temperature–entropy relation, because the electron contribution depends differently on temperature than the nucleon kinetic contribution. The electron fraction on the other hand is set by the symmetry energy. These effects, which are independent from the used energy–momentum relation, can be identified by comparing different RMF models or the two LS EOS. For example, LS (220) shows less dependence on entropy than LS (180). The same result was found by O’Connor & Ott (2011). It could be due to the dominance of the LS (220) EOS by interactions compared to the kinetic contribution. For the RMF models we see that FSUGold has the largest increase of the maximum mass at constant entropy. This can be related to its softer density dependence of the symmetry energy at high densities.

Independent of the detailed origin, with these results we have found a quantity which is directly correlated with the time until black hole formation: the maximum mass of proto-neutron stars, approximated by the “ $s = 4$ ” configuration. The time until black hole formation is monotonically increasing with the maximum masses of “ $s = 4$ ” proto-neutron stars with an approximately linear dependency. If for a known progenitor one could detect and follow the neutrino signal of the core-collapse supernova until black hole formation where the neutrino signal ceases, the correlation of Fig. 17 would give information about the maximum masses of such “ $s = 4$ ” configurations. This would represent a significant constraint for the nuclear EOS at finite entropy, complementary to observations of cold neutron stars.

The mass measurement of PSR J1614-2230 by Demorest et al. (2010) was a breakthrough for the physics of neutron stars. If a more massive pulsar was detected in the future, the constraints would become even more severe. However, pulsar mass measurements give always only a lower limit for the actual maximum mass. Contrary, with the black hole formation one has direct access to the (proto-neutron star) maximum mass. Furthermore, if we would know the real maximum mass of cold neutron stars, then one could use the neutrino signal to constrain the temperature dependence of the EOS. On the other hand, the correlation of Fig. 17 has also a lot of predictive power if it is combined with the mass constraint of pulsar PSR J1614-2230. All EOS with black crosses to the left of this line are not compatible with the observational data of PSR J1614-2230, because their maximum masses of cold neutron stars are too low. Thus

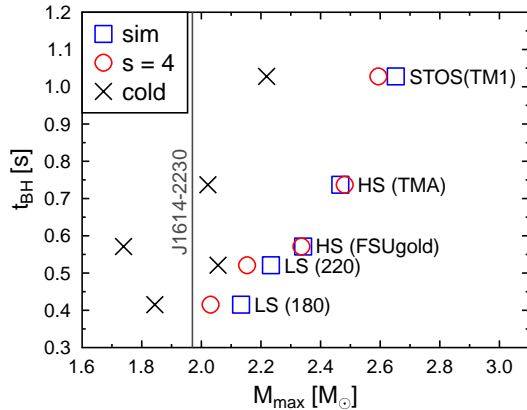


FIG. 17.— Time for the onset of collapse to a black hole for the $40 M_{\odot}$ progenitor of Woosley and Weaver (1995) with respect to different configurations of maximum gravitational masses for the investigated EOS. “cold”: static cold neutron stars at $T = 0.1$ MeV and beta-equilibrium without neutrinos. “ $s = 4$ ”: static proto-neutron stars at a constant entropy per baryon of $s = 4 k_B$ and beta-equilibrium without neutrinos. “sim”: the maximum gravitational masses found in the simulations. The vertical line shows the mass measurement of pulsar PSR J1614-2230 by Demorest et al. (2010).

we expect that the neutrino signal of such a black hole formation event from a massive $40 M_{\odot}$ progenitor will not be much shorter than 0.5 s. On the other hand, if the signal would end at $t_{pb} \ll 0.5$ s this would indicate the missing of important physics in the current models.

Finally, we have to make a remark of caution for the results of this section: for such high temperatures as encountered here, extensions of the EOS may become important, see, e.g., Oertel & Fantina (2010). Temperatures of 100 MeV are on the order of the pion mass, so a pion gas would form, and also muons and baryon resonances could give an important contribution to the EOS. In addition one has to be cautious using a non-relativistic EOS at such extreme conditions. It is not warranted that the EOS remains causal, i.e., that the speed of sound stays below the speed of light. We find that LS becomes acausal during the collapse to a black hole. However, we do not expect that our results will change qualitatively by these aspects, but still they should be studied more elaborately with extended EOS in the future.

5. SUMMARY AND CONCLUSIONS

We apply the new RMF EOS of the statistical model of Hempel & Schaffner-Bielich (2010) (HS) to core-collapse supernova simulations of 15 and $40 M_{\odot}$ progenitors. Our core-collapse model is based on general relativistic radiation hydrodynamics that employs three-flavor Boltzmann neutrino transport. The HS EOS include up to 8000 nuclei, based on experimentally known masses of Audi et al. (2003) and different theoretical nuclear structure calculations. Three different parameterizations of RMF interactions are applied, TM1, TMA, and FSUgold which govern the high-density behavior of the EOS. Regarding the nuclear matter properties and mass–radius relation of cold neutron stars, none of the HS EOS used here was able to fulfill all of the quoted experimental and observational constraints. The same holds for the commonly used EOS from H. Shen et al. (1998a) (STOS) and the EOS of Lattimer & Swesty (1991) (LS) with an incompressibility of 180 MeV (LS (180)). Furthermore,

we also include the LS EOS with an incompressibility of 220 MeV (LS (220)), which is in reasonable agreement with the considered constraints. The HS EOS tables are available for use and can be accessed from the home page given in footnote 1. Also routines are available which allow to calculate the abundances of all considered nuclei. Additional EOS tables for the NL3 (Lalazissis et al. 1997) and DD2 (Typel et al. 2010) RMF parameterizations can also be downloaded, which were not included in the present study. We remark that DD2 is in good agreement with the quoted experimental and observational constraints. In the future, the EOS tables will also be provided on the CompOSE(db) online platform of the CompStar research networking program.

We identify the most important differences between the HS EOS with the TM1 parameterization, the STOS EOS which is also based on TM1, and the LS (180) EOS by simulating the evolution of the $15 M_{\odot}$ progenitor. For the first time, two EOS are available which have identical nucleon interactions but a different description of the low-density phase where nuclei exist. In general one of the big advantages of the HS EOS, in comparison to LS and STOS, is the detailed information of the nuclear composition, the precise description of nuclei including shell effects, and the consideration of additional light nuclei. Regarding the first two aspects, the low-temperature HS EOS leads to a smooth transition from NSE to non-NSE at temperatures of about 0.5 MeV. There, HS matches the ideal gas of ^{56}Fe or ^{56}Ni (depending on the proton-to-baryon ratio) by construction, while LS and STOS produce artificial jumps, e.g., in internal energy. Also the agreement with the composition and the thermodynamic state of the progenitor was most satisfactory with HS. In the same sense, the HS EOS is well suited to be connected to explosive nucleosynthesis calculations, as it naturally gives a realistic seed distribution. Obviously, this is true for all NSE models which employ experimental nuclear binding energies, but the HS EOS tables also cover all densities and temperatures relevant for supernova simulations, which is not typical for most of the NSE models.

During the collapse we observe that HS (TM1) gives significantly smaller nuclei than STOS (TM1), leading to a stronger deleptonization and a lower electron fraction in the core. Contrary, the lower free proton fraction in the outer layers using HS caused less electron captures there. This illustrates impressively the sensitivity of the core-collapse simulation to slight changes of the nuclear composition. The electron captures in HS are less energetic, partly due to the use of real nucleon masses in the EOS, which therefore contain the proton-to-neutron rest-mass difference. During the collapse HS leads therefore to less entropy generation in the center compared with STOS.

The collapse phase is dominated by heavy nuclei. We investigated the nuclear distributions and identified a visible effect of neutron magic shells in the nuclear composition, leading, e.g., to several peaks in the mass distributions, which cannot be captured by the SNA. Interestingly, closed neutron shells also have an influence on the electron fraction profiles. In the innermost zones the nuclear distributions become very broad during collapse, due to the large compression heating. It would be a very appealing extension of the HS EOS model to calculate

weak reaction rates with the nuclear distributions of the EOS. Here, we only considered the average heavy nucleus in combination with the reaction rates of Bruenn (1985).

The appearance of additional light nuclei, which so far were not implemented in EOS tables for core-collapse supernovae, was investigated in detail. The formation of weakly bound light nuclei is driven by entropy. They are formed in the supernova by an interplay of density and temperature, where the temperature has to be high enough to suppress the role of differences in binding energies. We find that during the early collapse phase, the commonly used approximation to consider only alpha particles of all possible light nuclei is acceptable. However, already a few milliseconds before bounce temperatures are sufficiently high so that additional light nuclei can be even more abundant than alpha particles. When the shock runs through the infalling matter the well-known dissociation of heavy nuclei occurs. In the present article we further show that a significant fraction of light nuclei, e.g., ^2H , ^3H , ^3He , and Li , forms in the hot dissociated matter between the shock and the core of the proto-neutron star. These light nuclei remain there also in the post-bounce phase. For the inner layers of the proto-neutron star envelope, where matter is very asymmetric, tritium gives the largest contribution. In the outer layers below the shock, deuterium plays the most important role. We remark that these results for light nuclei obtained with the HS EOS are in qualitative agreement with expectations from the quantum many-body approaches of Röpke (2011) and Typel et al. (2010) (see Hempel et al. (2011)) and the previous study of Sumiyoshi & Röpke (2008).

In the present article, we simplified the neutrino reactions with light nuclei by treating all of them as alpha particles, i.e., we only considered elastic neutral-current reactions. However, light nuclei have low binding energies, except alpha particles. Because of the lower binding energies we expect that weak reactions with the other light nuclei will be different compared to the weak reactions with alpha particles. Some aspects may resemble the reactions with free nucleons. For example, also electron captures or break-up reactions of the deuteron are likely to occur. Until 50 ms post bounce the abundances of deuterons and tritons close to the shock are comparable to the ones of free protons. Thus, there may be an influence of light nuclei on neutrino heating during the early post-bounce phase. However, the fractions of light nuclei in the heating region decrease in the subsequent evolution. The largest fractions of light nuclei are then found below the neutrinospheres. Thus for the later post-bounce evolution cooling may be affected rather than heating. More detailed studies are required to answer to which extent light nuclei can contribute to the neutrino heating and cooling and possibly on the explosion dynamics. We see the consistent implementation of weak processes with light nuclei in the neutrino transport of core-collapse supernova simulations as an interesting task for future studies.

Regarding the hydrodynamic behavior of the new HS (TM1) EOS, we observed that it leads to a more compact proto-neutron star with slightly higher temperatures than with STOS (TM1). This is a result of the different description of the non-uniform nuclear matter phase, giving the appearance of light nuclei and smaller

heavy nuclei, which in turn leads to lower central electron fractions in the simulations. During the post-bounce evolution, the differences between HS (TM1), LS (180), and STOS (TM1) reduce. However, the much softer LS (180) EOS has significantly higher central temperatures and densities, and hence the standing accretion shock contracts faster. We arrive at the general conclusion that the model for low-density nuclear matter, where nuclei exist, and the implemented nuclear degrees of freedom are as important as the description of the nuclear interactions around and above saturation density.

We also compare the evolution of neutrino luminosities and mean energies for the different EOS, for the 15 M_{\odot} model. The soft LS (180) EOS leads to high neutrino fluxes and mean energies. Although STOS (TM1) and HS (TM1) are based on the same RMF parameterization, the larger deleptonization for HS results in larger neutrino fluxes and mean energies than STOS, emphasizing our statement above. The neutrino signatures are related to the evolution of the neutrinospheres which are located at the proto-neutron star surface. For LS (180) the proto-neutron star contracts fastest with highest temperatures and Y_e obtained, while STOS and HS have significantly longer contraction times especially after 300 ms post bounce. However, the differences obtained in the neutrino luminosities and mean energies are rather small. Therefore for such intermediate-mass progenitors, very precise neutrino observations of a possible future galactic supernova were required to constrain the nuclear EOS further. Note, this statement remains only valid if EOS effects are not affected significantly by the explosion, which is expected to occur for such a progenitor.

Pronounced EOS effects are found for the neutrino signal of the core-collapse supernovae of a 40 M_{\odot} progenitor. We confirmed the results of other studies that μ/τ -neutrinos carry an important signature of the EOS, namely, the temperatures reached inside the proto-neutron star, which are connected to the stiffness around saturation density. However, the most prominent EOS aspect related to the neutrino signal of such massive progenitors is the time until black hole formation. We found that it is dictated by the global behavior of the EOS and not by single EOS parameters. We showed that the correlation between time until black hole formation and maximum mass of cold neutron stars, found in previous EOS studies, does not hold for the extended set of EOS investigated here. Using the two non-relativistic LS EOS, the collapse to the black hole takes place systematically earlier than with the RMF EOS, even if the LS EOS have larger maximum masses for cold neutron stars. This interesting result was explained by the different response to finite temperature. For the RMF EOS a significantly larger increase of the maximum masses at finite entropy was observed than for the LS EOS. The states at the beginning of black hole formation in the simulations could be approximated by hydro-static configurations of proto-neutron stars at a constant entropy per baryon of $s = 4 k_B$. The resulting maximum masses agreed with the results from the simulations. We found a new monotonic correlation between the time until black hole formation and the maximum masses of these proto-neutron star configurations. From this correlation and the maximum mass constraint from Demorest et al. (2010), we

predict that the neutrino signal of a core-collapse supernova of a $40 M_{\odot}$ progenitor should last at least for 0.5 s starting at bounce, until the black hole forms. If such an event was measured in the future, the correlation would provide the maximum mass of proto-neutron stars at constant entropy. This would represent a significant constraint for the nuclear EOS at finite entropy, complementary to observations of cold neutron stars. In combination with the existing knowledge about the maximum mass of cold neutron stars this would give information about the temperature dependency of the EOS.

The EOS can also affect the explosion dynamics. In general, soft EOS lead to a stronger initial shock acceleration where higher matter velocities are obtained in comparison to stiff EOS (Baron et al. 1985a,b; Bruenn 1989). Therefore soft EOS result in a more optimistic situation with respect to the initial energetics at shock breakout shortly after bounce. This was confirmed in the present study, where the highest matter velocities for the bounce shock were encountered for the extremely soft LS EOS, and the lowest for the stiff TM1 EOS. Furthermore, although based on the same RMF parameterization TM1, STOS and HS have different shock energetics at shock breakout shortly after core bounce, due to the different description of nuclear matter below saturation density, and the resulting different deleptonization during the collapse. However, the situation becomes more similar after the bounce shocks have stalled. The initial dynamical advantage of a soft EOS is lost with time. It nevertheless leads to a more extended heating region between the neutrinospheres and the standing bounce shock. The in-

fluence of the EOS on explosions has been investigated in Marek & Janka (2009) based on simulations in axial symmetry. It would be an interesting follow-up project to perform a similar EOS comparison, as was done here, in multi-dimensional simulations, to further tackle the explosion mechanism of core-collapse supernovae.

ACKNOWLEDGEMENTS

We want to thank R. Käppeli, A. Arcones, A. Perego, S. Typel and G. Röpke for helpful discussions. Furthermore we thank S. Typel and A. Arcones for proofreading the manuscript and their useful comments. We are also grateful to X. Roca-Maza, L. Geng, G. Lalazissis and P. Ring for providing the nuclear mass tables used in the HS EOS. M.H. is supported by the High Performance and High Productivity Computing Project (HP2C), and the Swiss National Science Foundation (SNF) under project number no. 200020-132816/1. T.F. is funded by HIC for FAIR project no. 62800075 and the SNF under project no. PBBSP2-133378. J.S.-B. is supported by the German Research Foundation (DFG) within the framework of the excellence initiative through the Heidelberg Graduate School of Fundamental Physics. M.L. is funded by the SNF grant no. PPOOP2-124879/1. The authors are additionally supported by CompStar, a research networking program of the European Science Foundation (ESF). M.L. and M.H. are also grateful for participating in the EuroGENESIS collaborative research program of the ESF and the ENSAR/THEXO project.

REFERENCES

- Aparicio, J. M. 1998, *ApJS*, 117, 627
 Arcones, A., Martínez-Pinedo, G., O'Connor, E., Schwenk, A., Janka, H.-Th., Horowitz, C. J. & Langanke, K. 2008, *Phys. Rev. C*, 78, 015806
 Arcones, A., Martínez-Pinedo, G., Roberts, L. F. & Woosley S. E. 2010, *A&A*, 522, A25
 Audi, G., Wapstra, H. A. & Thibault C. 2003, *Nucl. Phys. A*, 729, 337
 Baron, E. Cooperstein, J. & Kahana S. 1985a *Nucl. Phys. A*, 440, 744
 Baron, E., Cooperstein, J. & Kahana, S. 1985b *Phys. Rev. Lett.*, 55, 126
 Bethe H. A. & Wilson, J R. 1985, *ApJ*, 295, 14
 Blinnikov, S.I., Panov, I. V., Rudzsky, M. A. & Sumiyoshi, K. 2011, *A&A*, 535, A37
 Bondorf, S. P., Botvina, A. S., Iljinov, A. S., Mishustin, I. N. & Snenpen, K. 1995, *Phys. Rep.*, 257, 133
 Botvina, A. S. & Mishustin, I. N. 2004, *Phys. Lett. B*, 584, 233
 Botvina, A. S. & Mishustin, I. N. 2010, *Nucl. Phys. A*, 843, 98
 Bruenn, S. W. 1985, *ApJS*, 58, 771
 Bruenn, S. W. 1989, *ApJ*, 341, 385
 Bruenn, S. W., Dirk, C. J., Mezzacappa, A., Hayes, C. J., Blondin, J. M., Hix, W. R. & Messer, O. E. B. 2006, *J. Phys.: Conf. Ser.*, 46, 393
 Buras, R., Janka, H.-Th., Keil, M. Th., Raffelt, G. G. & Rampp, M. 2003, *ApJ*, 587, 320
 Burrows, A. & Lattimer, J. M. 1984, *ApJ*, 285, 294
 Burrows, A., Livne, E., Dessart, L., Ott, C. D. & Murphy, J. 2006, *ApJ*, 640, 878
 Burrows, A., Livne, E., Dessart, L., Ott, C. D. & Murphy, J. 2007, *ApJ*, 655, 416
 Carbone, A., Colò, G., Bracco, A., Cao, L. G., Bortignon, P. F., Camera, F. & Wieland, O. 2010, *Phys. Rev. C*, 81, 041301
 Chen, L. 2012, *Science China Phys. Mech. Astron.*
 Demorest, P. B., Pennucci, T., Ransom, S. M., Roberts, M. S. E. & Hessels, J. W. T. 2010, *Nature*, 467, 1081
 Fáil, G. & Randrup, J. 1982, *Nucl. Phys. A*, 381, 557
 Fischer, T., Whitehouse, S. C., Mezzacappa, A., Thielemann, F.-K. & Liebendörfer, M. 2009, *A&A*, 499, 1
 Fischer, T., Whitehouse, S. C., Mezzacappa, A., Thielemann, F.-K. & Liebendörfer, M. 2010, *A&A*, 517, A80
 Fischer, T., Sagert, I., Pagliara, G., Hempel, M., Schaffner-Bielich, J., Rauscher, T., Thielemann, F.-K., Käppeli, R., Martínez-Pinedo, G. & Liebendörfer M. 2011, *ApJS*, 194, 39
 Furusawa, S., Yamada, S., Sumiyoshi, K. & Suzuki, H. 2011, *ApJ*, 738, 178
 Geng, L., Toki, H. & Meng, J. 2005, *Prog. Theor. Phys.*, 113, 785
 Goldreich, P. & Weber, S. V. 1980, *ApJ*, 238, 991
 Gong, Z., Zejda, L., Däppen, W. & Aparicio, J. M. 2001, *Comput. Phys. Commun.*, 136, 294
 Gross, D. H. E. 1990, *Rep. Prog. Phys.*, 53, 605
 Hannestad, S. & Raffelt, G. G. 1998, *ApJ*, 507, 339
 Heckel, S., Schneider, P. P. & Sedrakian, A. 2009, *Phys. Rev. C*, 80, 015805
 Hempel, M., & Schaffner-Bielich, J. 2010, *Nucl. Phys. A*, 837, 210
 Hempel, M., Schaffner-Bielich, J., Typel, S. & Röpke, G. 2011, *Phys. Rev. C*, 84, 055804
 Herant, M., Benz, W., Hix, W. R., Fryer, C. L. & Colgate, S. A. 1994, *ApJ*, 435, 339
 Hix, W. R., Messer, O. E. B., Mezzacappa, A., Liebendörfer, M., Sampaio, J., Langanke, K., Dean, D. J. & Martínez-Pinedo, G. 2003, *Phys. Rev. Lett.*, 90, 201102
 Horowitz, C. J. & Piekarewicz, J. 2001, *Phys. Rev. Lett.*, 86, 5647
 Horowitz, C. J. & Schwenk, A. 2006, *Nucl. Phys. A*, 776, 55
 Ishizuka, C., Ohnishi, A., & Sumiyoshi, K. 2003, *Nucl. Phys. A*, 723, 517
 Ishizuka, C., Ohnishi, A., Tsubakihara, K., Sumiyoshi, K. & Yamada, S. 2008, *J. Phys. G: Nucl. Phys.*, 35, 085201
 Janka, H.-Th. & Mueller, E. 1996, *A&A*, 306, 167
 Kitaura, F.-S., Janka, H.-Th. & Hillebrandt, W. 2006, *A&A*, 450, 345
 Koonin, S. E. & Randrup, J. 1987, *Nucl. Phys. A*, 474, 173
 Lalazissis, G. A., König, J. & Ring, P. 1997, *Phys. Rev. C*, 55, 540
 Langanke, K., Martínez-Pinedo, G., Sampaio, J. M., Dean, D. J., Hix, W. R., Messer, O. E. B., Mezzacappa, A., Liebendörfer, M., Janka, H.-Th. & Rampp M. 2003, *Phys. Rev. Lett.*, 90, 241102

- Langanke, K., Martínez-Pinedo, G., Müller, B., Janka, H.-Th., Marek, A., Hix, W. R., Juodagalvis, A. & Sampaio, J. M. 2008, *Phys. Rev. Lett.*, 100, 011101
- Lattimer, J. M. & Swesty, D. F. 1991, *Nucl. Phys. A*, 535, 331
- LeBlanc, J. M. & Wilson, J. R. 1970, *ApJ*, 161, 541
- Liebrandt, M., Mezzacappa, A., Thielemann, F.-K., Messer, O. E. B., Hix, W. R. & Bruenn, S. W. 2001, *Phys. Rev. D*, 63, 103004
- Liebrandt, M., Rosswog, S. & Thielemann, F.-K. 2002, *ApJS*, 141, 229
- Liebrandt, M., Messer, O. E. B., Mezzacappa, A., Bruenn, S. W., Cardall, C. Y. & Thielemann, F.-K. 2004, *ApJS*, 150, 263
- Liebrandt, M. 2005, *ApJ*, 633, 1042
- Liebrandt, M., Rampp, M., Janka, H.-Th. & Mezzacappa, A. 2005, *ApJ*, 620, 840
- Marek, A. & Janka, H.-Th. 2009, *ApJ*, 694, 664
- Martínez-Pinedo, G., Liebrandt, M. & Frekers, D. 2006, *Nucl. Phys. A*, 777, 395
- Mezzacappa, A. & Bruenn, S. W. 1993a, *ApJ*, 405, 637
- Mezzacappa, A. & Bruenn, S. W. 1993b, *ApJ*, 405, 669
- Mezzacappa, A. & Bruenn, S. W. 1993c, *ApJ*, 410, 740
- Mezzacappa, A. & Messer, O. E. B. 1999, *J. Comput. Appl. Math.*, 109, 281,
- Miller, D. S., Wilson, J. R. & Mayle, R. W. 1993, *ApJ*, 415, 278
- Müller, B., Janka, H.-Th. & Dimmelmeier, H. 2010, *ApJS*, 189, 104
- Nadyozhin, D. K. & Yudin, A. V. 2004, *Astron. Lett.*, 30, 634
- Nadyozhin, D. K. & Yudin, A. V. 2005, *Astron. Lett.*, 31, 271
- Nakamura, S. X., Sumiyoshi, K. & Sato, T. 2009, *Phys. Rev. C*, 80, 035802
- Nakazato, K., Sumiyoshi, K. & Yamada, S. 2008, *Phys. Rev. D*, 77, 103006.
- Natowitz, J. B., Röpke, G., Typel, S., Blaschke, D., Bonasera, A., Hagel, K., Klähn, T., Kowalski, S., Qin, L., Shlomo, S., Wada, R., & Wolter, H. H. 2010, *Phys. Rev. Lett.*, 104, 20250
- Newton, W. G. & Stone, J. R. 2009, *Phys. Rev. C*, 79, 055801
- Nomoto, K. 1983, in IAU Symp. 101, Supernova Remnants and their X-ray Emission, ed. J. Danziger & P. Gorenstein (Cambridge: Cambridge Univ. Press), 139
- Nomoto, K. 1984, *ApJ*, 277, 791
- Nomoto, K. 1987, *ApJ*, 322, 206
- O'Connor, E. & Ott, C. D. 2011, *ApJ*, 730, 70
- O'Connor, E., Gazit, D., Horowitz, C. J., Schwenk, A. & Barnea, N. 2007, *Phys. Rev. C*, 75, 055803
- Oertel, M. & Fantina, A. 2010, in SF2A-2010: Proc. Annual Meeting of the French Society of Astronomy and Astrophysics, ed. S. Boissier, M. Heydari-Malayeri, R. Samadi, & D. Valls-Gabaud, 185
- Piekarewicz, J. 2004, *Phys. Rev. C*, 69, 041301
- Piekarewicz, J. 2007, *Phys. Rev. C*, 76, 064310
- Piekarewicz, J. 2010, *J. Phys. G: Nucl. Phys.*, 37, 064038
- Potekhin, A. Y. & Chabrier, G. 2010, *Contrib. Plasma Phys.*, 50, 82
- Potekhin, A. Y., Chabrier, G., Chugunov, A. I., Dewitt, H. E. & Rogers, F. J. 2009, *Phys. Rev. E*, 80, 047401
- Raduta, A. R. & Gulminelli, F. 2010, *Phys. Rev. C*, 82, 065801
- Ravenhall, D. G., Pethick, D. J. & Wilson, J. R. 1983, *Phys. Rev. Lett.*, 50, 2066
- Roca-Maza, X. & Piekarewicz, J. 2008, *Phys. Rev. C*, 78, 025807
- Roca-Maza, X., Centelles, M., Viñas, X. & Warda, M. 2011, *Phys. Rev. Lett.*, 106, 252501
- Röpke, G. 1984, *Wiss. Z. Univ. Rostock*, 33, 33
- Röpke, G. 2011, *Nucl. Phys. A*, 867, 66
- Sagert, I., Fischer, T., Hempel, M., Pagliara, G., Schaffner-Bielich, J., Mezzacappa, A., Thielemann, F.-K. & Liebrandt, M. 2009, *Phys. Rev. Lett.*, 102, 081101
- Sharma, M. M. 2009, *Nucl. Phys. A*, 816, 65
- Shen, G., Horowitz, C. J. & O'Connor, E. 2011a, *Phys. Rev. C*, 83, 065808
- Shen, G., Horowitz, C. J. & Teige, S. 2011b, *Phys. Rev. C*, 83, 035802
- Shen, H., Toki, H., Oyamatsu, K. & Sumiyoshi, K. 1998a, *Prog. Theor. Phys.*, 100, 1013
- Shen, H., Toki, H., Oyamatsu, K. & Sumiyoshi, K. 1998b, *Nucl. Phys. A*, 637, 435
- Shen, H., Toki, H., Oyamatsu, K. & Sumiyoshi, K. 2011, *ApJS*, 197, 20
- Shlomo, S., Kolomietz, V. M. & Colò, G. 2006, *Eur. Phys. J. A*, 30, 23
- Souza, S. R., Steiner, A. W., Lynch, W. G., Donangelo, R. & Farniano, M. A. 2009, *ApJ*, 707, 1495
- Steiner, A. W., Lattimer, J. M. & Brown, E. F. 2010, *ApJ*, 722, 33
- Sugahara, Y. & Toki, H. 1994, *Nucl. Phys. A*, 579, 557
- Sumiyoshi, K. & Röpke, G. 2008, *Phys. Rev. C*, 77, 055804
- Sumiyoshi, K., Yamada, S. & Suzuki, H. 2007, *ApJ*, 667, 382
- Sumiyoshi, K., Yamada, S. & Suzuki, H. 2008, *ApJ*, 688, 1176
- Swesty, F. D. & Myra, E. S. 2005, in Open Issues in Core Collapse Supernova Theory, ed. A. Mezzacappa & G. M. Fuller, 176
- Timmes, X. F. & Arnett, D. 1999, *ApJS*, 125, 277
- Todd-Rutel, B. G. & Piekarewicz, J. 2005, *Phys. Rev. Lett.*, 95, 122501
- Toki, H., Hirata, D., Sugahara, Y., Sumiyoshi, K. & Tanihata, I. 1995, *Nucl. Phys. A*, 588, 357
- Tsang, M. B., Zhang, Y., Danielewicz, P., Farniano, M., Li, Z., Lynch, W. G. & Steiner, A. W. 2009, *Phys. Rev. Lett.*, 102, 122701
- Typel, S. 2005, *Phys. Rev. C*, 71, 064301
- Typel, S., Röpke, G., Klähn, T., Blaschke, D., & Wolter, H. H. 2010, *Phys. Rev. C*, 81, 015803
- Woosley, S. E. & Weaver, T. A. 1995, *ApJS*, 101, 181
- Woosley, S. E., Heger, A. & Weaver, T. A. 2002, *Rev. Mod. Phys.*, 74, 1015
- Yudin, A. V. 2011, *Astron. Lett.*, 37, 576